Macroscopic relations for microscopic properties at the interface between solid substrates and dense fluids

Antonio Russo, Miguel A. Durán-Olivencia, Serafim Kalliadasis (iD), and Remco Hartkamp (iD)

View Online   Export Citation   CrossMark

Macroscopic relations for microscopic properties at the interface between solid substrates and dense fluids

View Online   Export Citation   CrossMark

Antonio Russo,[1] Miguel A. Durán-Olivencia,[1] Serafim Kalliadasis,[1] (ID) and Remco Hartkamp[2,a] (ID)

AFFILIATIONS

[1] Department of Chemical Engineering, Imperial College London, London SW7 2WZ, United Kingdom

[2] Process and Energy Department, Delft University of Technology, Leeghwaterstraat 39, 2628 CB Delft, The Netherlands

[a] Electronic mail: r.m.hartkamp@tudelft.nl

ABSTRACT

Strongly confined fluids exhibit inhomogeneous properties due to atomistic structuring in close proximity to a solid surface. State variables and transport coefficients at a solid-fluid interface vary locally and become dependent on the properties of the confining walls. However, the precise mechanisms for these effects are not known as of yet. Here, we make use of nonequilibrium molecular dynamics simulations to scrutinize the local fluid properties at the solid-fluid interface for a range of surface conditions and temperatures. We also derive microscopic relations connecting fluid viscosity and density profiles for dense fluids. Moreover, we propose empirical ready-to-use relations to express the average density and viscosity in the channel as a function of temperature, wall interaction strength, and bulk density or viscosity. Such relations are key to technological applications such as micro-/nanofluidics and tribology but also natural phenomena.

I. INTRODUCTION

Fluid interfaces are ubiquitous in a wide spectrum of natural phenomena and technological applications, from the wetting properties of plant leaves[1] and insects walking and jumping on water[2] to recent technological advances in micro-/nanofluidics,[3,4] design of surfaces with controllable wetting properties,[5–8] colloidal science,[9,10] bioengineering,[11–13] sensing,[14] and biomimetics.[15,16] All these demand a molecular-level understanding of the fundamental physical properties of matter on interfaces. Moreover, integration and scaling out of the associated products, processes, and devices require appropriate macroscopic relations able to integrate a microscopic description of fluid properties at interfaces. Despite significant efforts (e.g., Refs. 17–20), such macroscopic relationships are yet to be obtained for general conditions, and studies on interfacial phenomena often rely on simplistic assumptions. Experimental observations at the nanoscale, often with a technique such as scanning tunneling microscopy, are complex and mostly limited to static properties. On the other hand, continuum hydrodynamic models based on the Navier-Stokes equations are not able to

predict molecular-scale phenomena, where the discrete nature of matter comes to the fore. More refined continuum hydrodynamic models, such as those in the framework of dynamic density-functional theory, take into account fluid-fluid and fluid-solid interactions through a mean field approach (e.g., Refs. 22–24). However, such models still involve certain unresolved closures, such as the functional dependence of viscosity on density. In contrast to the top-down approach of continuum methods, molecular dynamics (MD) simulations require no prior assumption on the local fluid properties. As such, MD is a powerful toolbox to gain insight into the physical properties of fluids, often intertwined, and the pertinent microscopic-macroscopic relationships.

Local viscosity remains one of the most elusive physical properties. The first successful attempt to model viscosity is due to Maxwell in 1860.[25] Using the internal friction of a dilute gas predicted from kinetic theory,[26] Maxwell concluded that the internal friction of a gas is independent of density. This was later confirmed by Chapman[27] and Enskog.[28] Enskog subsequently showed that, unlike dilute gases, the viscosity of dense gases exhibits both density and temperature dependencies.[29] Since then, several researchers

have tried to generalize Enskog's theory to inhomogeneous systems by utilizing both theoretical and numerical studies, with mixed success. A study by Din and Michaelides[18] provided a theoretical framework to model the viscosity of strongly inhomogeneous gases. However, the authors concluded that this formulation is able to approximate the viscosity profile of a more complex fluid, such as Lennard-Jones (LJ), only qualitatively. Zhang et al.[30] proposed an effective space-dependent viscosity, derived from a nonlocal linear hydrodynamic model, which constitutes a generalization of Newton's law. Unfortunately, Zhang et al.'s approach does not allow for the derivation of a general simple formula for the viscosity as a function of the density. Both numerical and theoretical studies of transport properties (viscosity, thermal conductivity, and diffusion coefficient) in confined geometries can be found in Refs. 31–33. These works mainly deal with the effects of walls on the fluid structure and fluid properties for different nanochannel widths. Recently, Hoang et al.[21,34,35] proposed adopting local average-density models combined with appropriate weight functions to consider nonlocal contributions to the viscosity. This empirical method leads to viscosity profiles in line with MD results in the case of fairly adsorbent narrow pores.

Despite considerable efforts to consider the effects of temperature and wall-interaction strength on local viscosity, a generic model remains elusive. Here, we use nonequilibrium MD simulations of a LJ fluid sheared between two parallel walls to scrutinize inhomogeneous interfacial fluid properties. Of particular interest here is shear viscosity. We adopt two approaches. First, we propose a generalization of the relation for the viscosity profile that was recently proposed by Morciano et al.[36] This generalized relation is validated for a range of interfacial conditions and temperatures. Second, we define a region in which wall effects are predominant and use this definition to calculate the average properties of the confined fluid. The study of fluid properties in this interfacial region provides ready-to-use relations that can be employed in the design and analysis of microfluidic devices, where solid-fluid interfaces play an important role.

In Sec. II, we present the simulation details. In Sec. III, we discuss how local fluid properties are calculated. The results are presented in Sec. IV. Conclusions and suggestions for future developments are offered in Sec. V.

II. SIMULATION DETAILS

In this study, we simulate Couette flow, produced by shearing two parallel atomistic walls with a fluid sandwiched between them, as shown in Fig. 1. The fluid and wall atoms are modeled as LJ particles, representing a charge-neutral and inert material. The interaction between any two particles i and j is described by the two-body potential U_{LJ},

$$U_{LJ}(r_{ij}) = 4\,\epsilon_{LJ,ij}\left[\left(\frac{\sigma_{LJ,ij}}{r_{ij}}\right)^{12} - \left(\frac{\sigma_{LJ,ij}}{r_{ij}}\right)^{6}\right], \quad (1)$$

where $r_{ij} = |\mathbf{r}_i - \mathbf{r}_j|$ is the distance between the particles, $\epsilon_{LJ,ij}$ is the depth of the potential well, and $\sigma_{LJ,ij}$ is the finite atom-atom distance at which the potential is zero. The interaction potential is truncated at a cutoff radius, r_c, such that $U_{LJ}(r_{ij} \ge r_c) = 0$. Hereafter, all physical
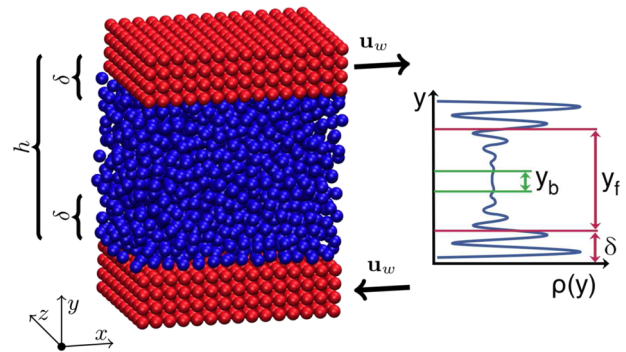

FIG. 1. Nonequilibrium MD setup for the study of a sheared fluid (shown in blue). The walls (shown in red) at a constant distance $h = 13.0\sigma_{LJ}$ move in opposite directions at constant velocity $\mathbf{u}_w$. The parameter δ defines the confined regions at the solid interfaces where the strong interactions reduce the mobility of fluid particles, and $y_f = h - 2\delta$ is its complementary region. The bulk region, $y_b \simeq 4\sigma_{LJ}$, is defined as the part of the fluid where no significant layering is observed in the density profile.

quantities are expressed in reduced LJ units, and they are nondimensionalized with the fundamental quantities: σ_{LJ}, ϵ_{LJ}, and m, corresponding to distance, energy, and mass, respectively. For example, the characteristic time in reduced units becomes $\tau = \sqrt{\sigma_{LJ}^2 m/\epsilon_{LJ}}$. For the LJ potential parameters, the following values are adopted: $\epsilon_{LJ,f,f} = \epsilon_{LJ}$, $\epsilon_{LJ,f,w} = \{0.6, 1.0, 1.4\}\epsilon_{LJ}$, and $\sigma_{LJ,f,f} = \sigma_{LJ,f,w} = \sigma_{LJ}$. Furthermore, a cutoff radius $r_c = 3.5\sigma_{LJ}$ is employed. Without loss of generality, σ_{LJ}, ϵ_{LJ}, m, and the Boltzmann constant k_B are set equal to unity.

Figure 1 shows the simulation system. The accessible fluid domain (delimited by the center of the wall particles in direct contact with the fluid) is kept constant at $[15\sigma_{LJ}] \times [13\sigma_{LJ}] \times [10\sigma_{LJ}]$ throughout the simulations. Periodic boundary conditions are imposed along the x and z directions, while the fluid is enclosed in the y direction by parallel walls. A steady shear flow is generated by imposing equal and opposite velocities to the two walls along the x direction.[37] It should be noted that non-Newtonian effects (such as shear thinning) start to appear at high shear rate values.[17,38] To remain in the Newtonian regime, while obtaining a significant signal-to-noise ratio, we adopt a wall velocity $\mathbf{u}_w = 1.0$, producing average shear rates of 0.15.[17]

Under shear, viscous dissipation results in heat generation at a rate proportional to $\dot{\gamma}^2$. This heat can be dissipated by connecting either the walls or the fluid to a heat bath, with both approaches being widely used.[39] If heat is dissipated through the walls, the vibrations of wall particles are controlled via a thermostat. While such an approach is physically intuitive, it can give rise to considerable variations in the fluid temperature across the channel when heat is created at a faster rate than it is conducted and dissipated by the walls.[40] This scenario, which can occur at the large shear rates that are needed in nonequilibrium MD simulations to collect meaningful statistics, is not representative of the nearly constant temperature profile in typical nanofluidic or nanotribological applications,[41] performed at much lower shear rates.

Alternatively, the system temperature can be controlled by applying a thermostat directly to the fluid particles. In this way, it is possible to ensure an experimentally representative constant temperature across the channel, despite the much higher shear rate employed in simulations. Since this approach to control temperature does not require movement of wall particles, the wall can be modeled as a rigid entity. A key advantage of such a rigid-wall approach is that interactions between wall particles do not need to be calculated, thus considerably lowering the computational cost. In this work, walls are modeled as a rigid square lattice, with a lattice spacing of σ_{LJ}. We note that a fixed lattice enhances the fluid layering close to the walls, compared to the more disordered or flexible "soft" walls, thus the interfacial structure, depending strongly on the spring stiffness, as observed in Refs. [42]–[44].

The heating caused by shearing of the fluid is removed from the system by thermostatting the fluid particle velocities in the y and z directions. We adopt a Nosé-Hoover (NH) thermostat, which has been shown to perform well for weakly sheared systems and, unlike Langevin and dissipative particle dynamics thermostats, does not alter the value of the system's viscosity.[45] However, applying NH globally to the inhomogeneous fluid could be problematic, especially at high shear rates. Instead, we apply separate Nosé-Hoover[46–48] thermostats to 13 equally sized slabs of fluid perpendicular to the walls, as done in previous works[20,49] (more details and validation are provided in Appendix A). The fluid is simulated at constant temperatures, $1.0 \leq T \leq 4.0$.

The simulations are performed using the Large-Scale Atomic/ Molecular Massively Parallel Simulator (LAMMPS).[50] The equations of motion are integrated using the velocity-Verlet[51] algorithm, with a time step of $dt = 0.005\tau$.[52] A typical simulation consists of the following protocol. First, the system is relaxed at equilibrium conditions for 2×10^6 time steps. Then, a constant velocity is imposed on the walls, and a nonequilibrium steady state is reached after 2×10^6 time steps, ensured by convergence of the density and velocity profiles. Finally, a run of 2×10^6 time steps is performed, during which fluid particle positions and velocities are stored every 10^2 time steps for analysis and postprocessing.

III. ANALYSIS

For inhomogeneous systems, state variables and transport coefficients can vary in space such that microscopic fields need to be calculated as a function of position from the particle positions, velocities, and interactions. Two types of methods can be distinguished differing in the way they distribute the microscopic information in space.

The vast majority of studies divides the spatial domain into a finite number of bins and assigns the information on a particle to the bin in which the center of that particle resides. This approach is computationally cheap and convenient, but it disregards the finite particle size. Furthermore, when a particle resides anywhere within the confines of a bin, its information is effectively assigned to the central position of a bin, thus potentially shifting the information. Such a shift, which is irreversible, can dramatically affect oscillatory fields, such as density and pressure profiles at the fluid-solid interface. This shift of information is averted in the limit of infinitesimally thin bins, but this would require infinitely long simulations to gather sufficient statistics in each bin. Apart from the shifting of data, the

discretization of spatial profiles renders it impossible to analytically calculate gradients of computed profiles, which instead demands an additional numerical approximation.

These limitations can be overcome by locally distributing the atomistic information via a smooth differentiable kernel, inspired by smoothed particle hydrodynamics.[53] In this approach, a macroscopic field $X(\mathbf{r}, t)$ is expressed as

$$X(\mathbf{r}, t) = \sum_i \chi_i \phi(\mathbf{r}_i(t) - \mathbf{r}), \qquad (2)$$

where χ_i is the information on interest of particle i at position $\mathbf{r}_i$ at time t, and ϕ is a kernel function, with the area under the kernel being unity. The most commonly used kernels are a piecewise constant, Gaussian, or polynomial function. These kernels will be briefly introduced below. For the purpose of this study, profiles are calculated as functions of one spatial coordinate y and the dependency on time is omitted. Instead, stored information is averaged under the ergodic assumption (i.e., for a given macroscopic property X, the ensemble average and time average are considered equivalent: $\langle X \rangle_{NVT} = \langle X \rangle_t$).

The piecewise constant function (mostly adopted in mesh-based approaches) is defined as

$$\phi(y_i - y) = \begin{cases} \frac{1}{2L_x L_z w} & \text{for} \|y_i - y\| < w, \\ 0 & \text{otherwise}, \end{cases} \qquad (3)$$

with L_x and L_z being the total system length along the x and z directions, respectively, and w being the half-width of the function. The Gaussian kernel is given by

$$\phi(y_i - y) = \begin{cases} \frac{1}{L_x L_z \sqrt{2\pi w^2}} e^{-\frac{\|y_i - y\|^2}{2w^2}} & \text{for} \|y_i - y\| < R_c, \\ 0 & \text{otherwise}, \end{cases} \qquad (4)$$

where w^2 is the variance. In addition, linear,[54] cubic,[55] and quartic[56] splines have been commonly used in the literature. A cubic spline is given by

$$\phi(y_i - y) = \begin{cases} \frac{1}{L_x L_z w}\left(1 - 3\frac{\|y_i - y\|^2}{w^2} + 2\frac{\|y_i - y\|^3}{w^3}\right) & \text{for} \|y_i - y\| < w, \\ 0 & \text{otherwise}, \end{cases} \qquad (5)$$

where w controls the width of the kernel.

The Gaussian kernel is more computationally expensive than a polynomial function and has no compact support as the Gaussian function never reaches zero. The latter issue can be easily overcome by appropriately truncating the function and then reweighing it so that the microscopic information is conserved. On the other hand, a main advantage of the Gaussian kernel is that it allows for calculating exactly the nth spatial derivative of a macroscopic field X as

$$\frac{dX^n(y)}{dy^n} = \left\langle \sum_i \chi_i \frac{d^n \phi(y_i - y)}{dy^n} \right\rangle_t. \qquad (6)$$

Equation (6) can also be applied to a polynomial, or "Lucy," kernel, for which the smoothness and the number of derivatives that can be taken are limited by the order of the polynomial, which also determines the computational cost of the kernel.

In Fig. 2(a), we compare, for a small toy system, the one-dimensional density profiles computed by using binning and different kernel-based methods. In the binning approach, the domain is divided into ten bins of equal width. The number density in a bin then equals the number of particles in that bin divided by its volume. As shown in the top panel of Fig. 2(a), the density peaks are shifted with respect to the particle centers. A second approach consists of adopting a meshfree discretization that employs piecewise constant, cubic, and Gaussian kernels. This method allows for an arbitrary number of computational points within the domain and, thus, a finer description of the density. The piecewise constant kernel assumes that all the information on a particle is homogeneously distributed across a width of $2w$. Consequently, the piecewise constant profile can still cause artificial density peaks, as seen on the right side of the middle panel of Fig. 2(a). On the contrary, both cubic and Gaussian kernels are able to provide a more accurate description of the local features characterizing the system density.

Various recent studies, especially in the areas of granular[57,58] and molecular simulations,[20,59,60] have reported how details of the kernel affect the calculated macroscopic profiles. For example, Weinhart et al.[57] found, using granular flow simulations, that the Gaussian smoothing parameter w should be small compared to the smallest length scale to be captured. In the case of confined LJ fluids, the smallest length scale of interest is approximately $0.9\sigma_{LJ}$, corresponding to the period of density oscillations near the channel wall.[61] In this study, we adopted a Gaussian kernel with $w = 0.1$, truncated at $6.5\sigma_{LJ}$ (half domain).

A. Density, momentum, and temperature

The density profile across the channel can be computed as

$$\rho(y) = \left\langle \sum_i m_i \phi(y_i - y) \right\rangle_t, \tag{7}$$
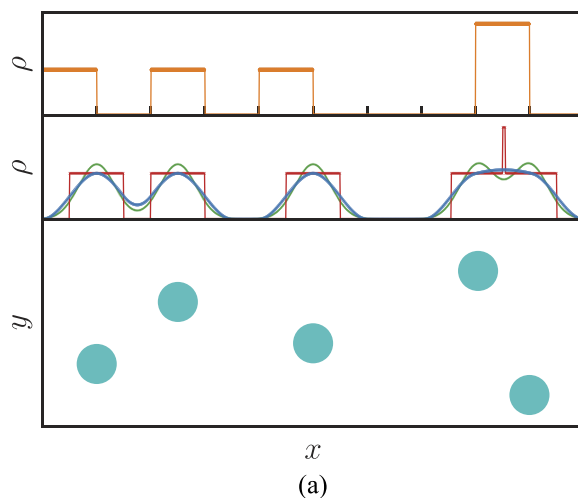
where m_i is the mass of particle i. In a similar fashion, the velocity profile is evaluated from the momentum $\mathbf{J}(y)$ and density profiles as

$$\mathbf{u}(y) = \frac{\mathbf{J}(y)}{\rho(y)} = \frac{\langle \sum_i m_i \mathbf{u}_i \phi(y_i - y) \rangle_t}{\rho(y)}, \tag{8}$$

where $\mathbf{u}_i$ is the velocity vector of particle i. From the mass density and the x-component of the momentum, it is possible to compute the shear rate profile by applying the quotient rule

$$\dot{\gamma}(y) = \frac{du_x(y)}{dy} = \frac{\rho(y)\frac{dJ_x(y)}{dy} - \frac{d\rho(y)}{dy}J_x(y)}{\rho(y)^2}, \tag{9}$$

where the two gradients in the numerator can be obtained analytically for differentiable kernels via Eq. (6).

To illustrate that gradients of macroscopic fields can be particularly sensitive to the method used to distribute information, we compare in Fig. 2(b) density and shear rate profiles for a sheared LJ fluid calculated with different kernels. The widths of the kernels are chosen such that they spread the data approximately equally. Although the density profiles are not significantly affected by the kernel's shape, the shear rate profile calculated with the piecewise constant kernel deviates from the other analytically differentiated profiles close to the walls.

In addition, the local temperature of the system can be evaluated as a function of particle fluctuation velocities $\mathbf{c}_i$ and the number density profile $n(y)$ as

$$T(y) = \frac{1}{3n(y)}\left\langle \sum_i m_i \mathbf{c}_i \cdot \mathbf{c}_i \, \phi(y_i - y) \right\rangle_t, \tag{10}$$

where the fluctuation velocity vector $\mathbf{c}_i = \mathbf{u}_i - \mathbf{u}(y_i)$ is the difference between the particle velocity $\mathbf{u}_i$ and the local streaming velocity vector $\mathbf{u}(y_i)$.
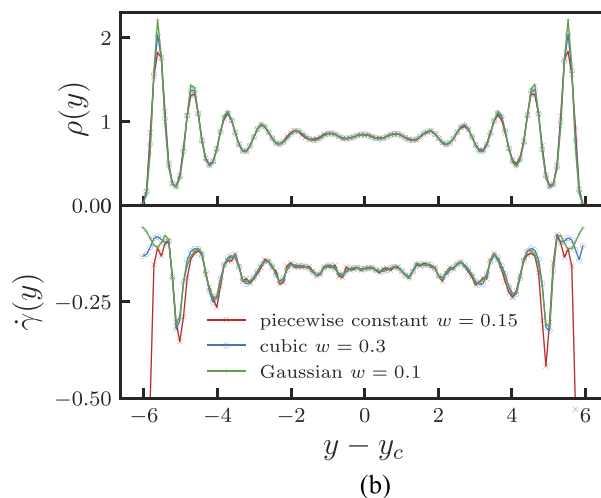

FIG. 2. (a) Density profiles of a toy system (bottom panel). The top panel shows the bins of width $w = 0.3$ employed to compute the density. The middle panel shows profiles computed using three different kernels: piecewise constant with $w = 0.15$ (red line), cubic with $w = 0.3$ (blue line), and Gaussian with $w = 0.1$ (green line). (b) Density and shear rate profile computed at $T = 1.0$ and $\epsilon_{LJ,f,w} = 1.0$ for three choices of kernel functions (piecewise constant, cubic, and Gaussian). The center of the channel positions is denoted by y_c.
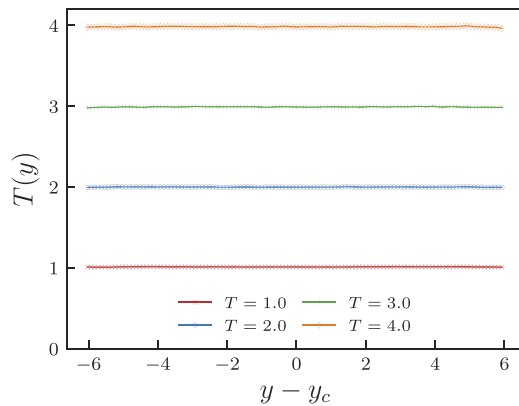
FIG. 3. Temperature profiles at different temperatures, $1.0 \leq T \leq 4.0$ for $\epsilon_{LJ,f,w}$ = 1.0.

Figure 3 shows the effectiveness of the local thermostatting strategy in maintaining a constant temperature across the channel, despite the large shear rate of 0.15. Figure 15 (Appendix A) reveals that the temperature exhibits spurious effects when a single thermostat is globally applied to the fluid or when the shear rate is much greater than 0.15.

B. Stress tensor

The stress tensor is computed via the Irving-Kirkwood-Noll formulation.[62] In this formulation, the six independent components of the symmetric stress tensor arise from a kinetic contribution, related to thermal motion, and a potential contribution, caused by interactions between particles

$$\boldsymbol{\sigma}(y) = \boldsymbol{\sigma}^k(y) + \boldsymbol{\sigma}^v(y). \tag{11}$$

The kinetic stress tensor is calculated from the thermal motion of the particles

$$\boldsymbol{\sigma}^k(y) = -\left\langle \sum_i m_i (\mathbf{u}_i - \mathbf{u}(y_i)) \otimes (\mathbf{u}_i - \mathbf{u}(y_i)) \, \phi(y_i - y) \right\rangle_t. \tag{12}$$

The potential stress tensor accounts for contributions due to interaction between particles

$$\boldsymbol{\sigma}^v(y) = -\left\langle \frac{1}{2} \sum_{i,j,j\neq i} \mathbf{F}_{i,j} \otimes (\mathbf{r}_i - \mathbf{r}_j) \, b_\phi(y; y_i, y_j) \right\rangle_t, \tag{13}$$

where $\mathbf{F}_{i,j}$ is the force acting on particle i due to particle j, and $b_\phi(y; y_i, y_j) = \int_{s=0}^1 \phi((1-s)y_i + sy_j - y)ds$ is the bond function.[63,64]

IV. RESULTS AND DISCUSSION

A. Density profile

The fluid structure density exhibits a rich behavior in the channel. The region at the center of the channel, of width approximately equal to $y_b \simeq 4\sigma_{LJ}$, does not show significant layering, and thus, it will be denoted as a bulk region. The density profiles in Fig. 4 reveal that the intensity of the density layering near the wall depends inversely on temperature and directly on $\epsilon_{LJ,f,w}$. On the other hand, the location of the layers remains unaffected, as it depends primarily on the wall structure and on the interaction length scale parameter σ, which are both identical for each of the simulations. The dense layers are equidistant, with a mean distance between adjacent peaks of about $l = 0.93$, consistent with Refs. 20 and 65, and in reasonable agreement with that predicted by kinetic theory $l \sim \left(\sqrt{2}\sigma_{LJ}\bar{\rho}\right)^{-1} = 0.88$. The density profiles obtained from MD are well approximated with the following exponential oscillatory relation:

$$\rho(y) = \rho_b \left(1 + A e^{-B(y-y_w)} \cos\left[\frac{2\pi}{l}(y - y_w) \right] \right), \tag{14}$$
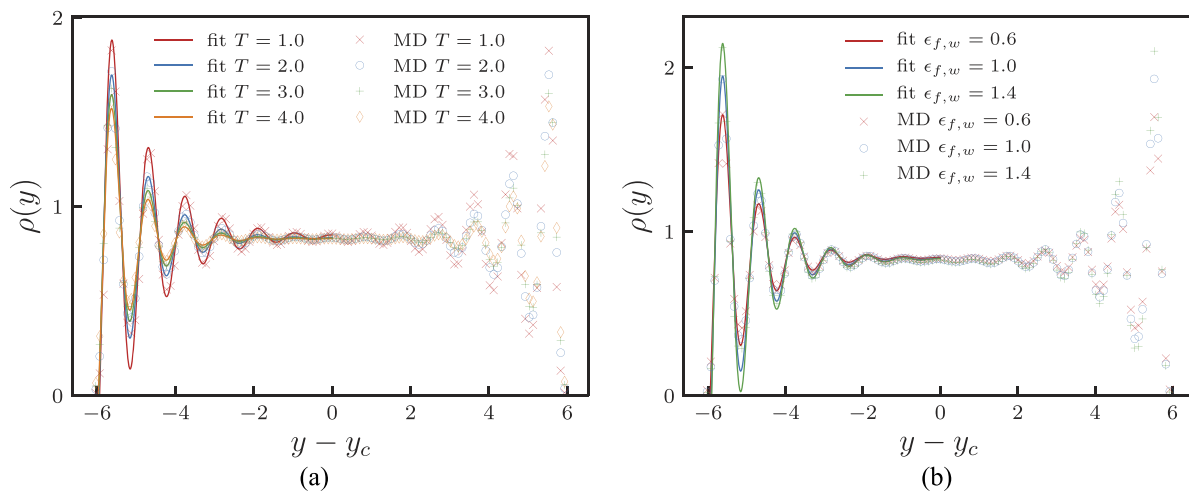

FIG. 4. (a) Density profile at different temperatures of the domain, $1.0 \leq T \leq 4.0$. (b) Density profile for different interaction potentials between walls and fluid, $\epsilon_{LJ,f,w}$ = 0.6, 1.0, 1.4. The markers represent the MD simulation results, while the fitting relation given by Eq. (14) is reported in solid lines.

where ρ_b is the density in the bulk region of the channel, the fitting parameter $A = A(\epsilon_{LJ,f,w}, T)$ represents the largest amplitude of the oscillations, and $B = B(\epsilon_{LJ,f,w}, T)$ indicates the decay away from the interface, located at y_w. It turns out that the amplitude is mainly dependent on the fluid-wall interactions and can be expressed as $A \sim 3.5 \, \epsilon_{LJ,f,w}^{0.5}$, whereas the decay parameter depends mostly on the temperature as $B \sim 0.85 \, T^{0.3}$. The comparison of Eq. (14) with MD data (fitting curves shown in Fig. 4) leads to relative errors ranging between 2% and 10%.

B. Standoff distance and confinement parameter

The density layering at the walls is a result of the competition between potential energy, which favors an ordered structure of the fluid, and particles' thermal energy. Following the work of Chiavazzo et al.,[66] we introduce the total energy as the sum of the kinetic energy and the potential energy relative to its value in the bulk region. The total energy profile in a channel is evaluated as

$$E(y) = U(y) + \alpha \frac{k_B T}{2}, \tag{15}$$

where $U(y)$ is the potential energy acting on the fluid particles due to the walls and the other fluid particles, and α indicates the fraction of the average thermal energy per particle available to escape the wall absorption. Because of the equipartition theorem, each degree of freedom has associated a kinetic energy of $k_B T/2$. Since particles in the proximity of a flat wall are able to overcome the potential energy barriers only along a single direction normal to the solid surface (representing half degree of freedom), α is taken to be equal to $1/2$.[66] A locally negative total energy indicates that the average kinetic energy of fluid particles is insufficient to escape the potential energy well. On the contrary, fluid particles in regions of positive total energy have enough energy to move freely and diffuse. Therefore, the local total energy can be used to distinguish between regions in which fluid particles are confined or free.

The potential energy $U(y)$ can be computed following two approaches. First, the effective potential energy, that takes into account both wall-fluid and fluid-fluid particles' interactions, can be calculated from the density profile at equilibrium according to the Boltzmann distribution[67,68]

$$U_{eff}(y) = -k_B T \log\left(\frac{\rho(y)}{\rho_b}\right), \tag{16}$$

where ρ_b is the bulk density. Alternatively, the potential energy landscape near an infinite lattice wall can be modeled analytically as[61]

$$U_{LJ_{10-4}}(y) = \frac{2\pi\rho_w \epsilon_{LJ,f,w}}{5}\left[2\left(\frac{\sigma_{f,w}}{y-y_w}\right)^{10} - 5\left(\frac{\sigma_{LJ,f,w}}{y-y_w}\right)^4\right], \tag{17}$$

where ρ_w is the number density of the walls. The latter expression has the advantage of providing an analytical form for the wall potential that is independent from the density profile. However, this approach neglects the influence of the interactions between fluid particles, thus potentially resulting in significant inaccuracies in the case of strong fluid-wall interaction.

The energy $E(y)$ gives access to two important quantities: the standoff distance and the confinement parameter. The standoff distance y_{min} is defined as the minimum distance that fluid particles can approach the wall

$$y_{min} = n_1 - y_w, \tag{18}$$

with n_i, $i = 1, \ldots, r$ being the roots of the function $E(y) = 0$ and y_w being the position of the first layer of wall particles. Given the steep potential energy profile near the wall, it can be seen that $U(y) \sim E(y)$ close to the walls. Consequently, the standoff distance can be readily obtained by finding the roots of $U_{LJ_{10-4}}(y) = 0$, rather than $E(y) = 0$. It follows that $y_{min} \sim (2/5)^{1/6} \sim 0.86$, as also verified in Wang and Hadjiconstantinou.[61] The comparison with our MD results shows that this approximation is able to accurately model the standoff distance within 3% error.

Chiavazzo et al.[66] introduced a way of estimating a confinement parameter δ,

$$\delta = n_r - y_w, \tag{19}$$

where y_w is the position of the wall. δ is defined as the distance from the wall within which the surface effects are significant. As such, it provides a quantitative means to identify two regions inside the channel: A confined one, where the influence of the wall is predominant, and a free region of width y_f, where particles are only marginally affected by the presence of the fluid-solid interface. Figure 5(a) depicts the total energy landscape $E(y)$ for two limiting cases: one with hydrophobic walls and the fluid temperature being high (weak layering) and the other with very hydrophilic walls and the fluid temperature being low (strong layering). For the sake of completeness, we also report the potential energy excess at the wall computed directly from interatomic interactions. The small discrepancy observed between the energy landscape computed from particle interactions, and the one obtained from the Boltzmann distribution does not significantly affect the value of the parameter δ. The standoff distance y_{min} and the confinement parameter δ are indicated for the latter case.

Figure 5(b) shows the parameter δ, computed with both approximations of $U(y)$, as a function of the Wall number $Wa = (\rho_{wall}\sigma_{LJ}^2\epsilon_{LJ,f,w})/(k_B T)$, which is a measure of the influence of the walls on the fluid.[61] The values of δ obtained for $U_{eff}(y)$ are, in most cases, greater than the ones obtained for $U_{LJ_{10-4}}(y)$, and, in both cases, δ increases with Wa. The greater values for δ obtained for $U_{eff}(y)$ indicate that correlations between fluid particles [which are not taken into account by $U_{LJ_{10-4}}(y)$] increase the region where the effect of the confinement is strong. Furthermore, δ calculated from $U_{LJ_{10-4}}(y)$ increases smoothly with Wa, whereas δ evaluated from $U_{eff}(y)$ shows a stepwise trend. This behavior is related to the number of fluid layers intercepted by the horizontal axis in the total energy profile.

C. Global density for a fluid in a confined geometry

Using the partitioning of the fluid domain into a confined region and a free region, we propose an analysis of the averaged fluid properties in these regions. First, we define the volume of the confined region for a channel with cross-sectional surface area S as $V_c = \delta(T, \epsilon_{LJ,f,w})S$, and consequently the free volume as
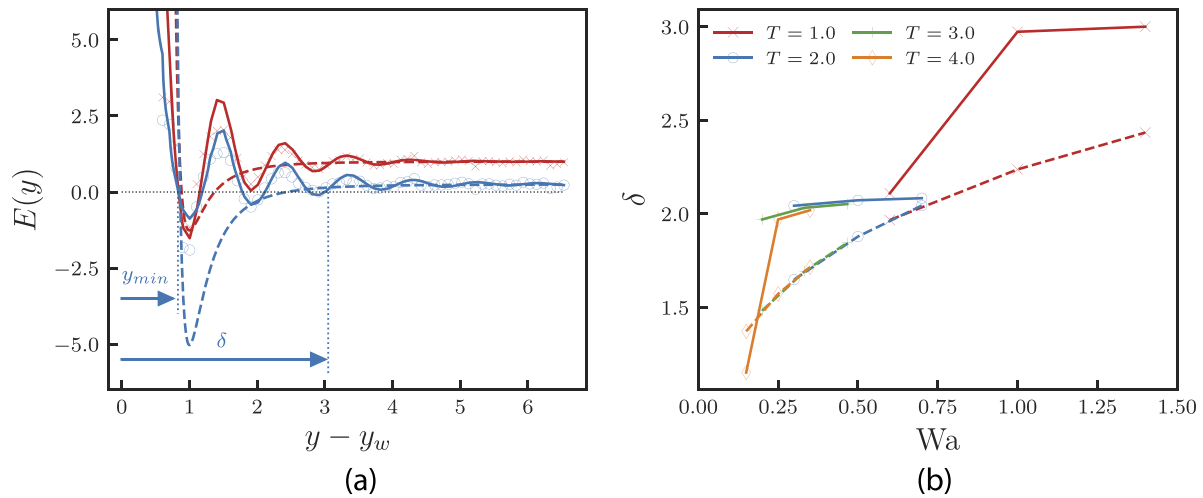
FIG. 5. (a) Interfacial energy profile computed with potential energy U_{eff} (solid lines) and $U_{LJ_{10-4}}(y)$ (dashed lines) in two representative cases, one with $\epsilon_{LJ,f,w} = 0.6$ and $T = 4.0$ (in red), the other with $\epsilon_{LJ,f,w} = 1.4$ and $T = 1.0$ (in blue). Markers represent the potential energy excess at the wall computed directly from interatomic interactions. The roots of this functions define y_{min} and δ parameters according to Eqs. (18) and (19). (b) The parameter δ as a function of the Wall number when computed from U_{eff} (solid lines) and from $U_{LJ_{10-4}}(y)$ (dashed lines).

$V_f = V_{tot} - V_c$, where V_{tot} is the total volume of the channel. The average confined density can then be computed as $\rho_c = \frac{1}{V_c} \int_{V_c} \rho(y) dV$ and the average free density as $\rho_f = \frac{1}{V_f} \int_{V_f} \rho(y) dV$. The behavior of these average densities relative to the bulk density ρ_b is shown in Fig. 6. It is evident that the average free density is approximately equal to the bulk density, regardless of the fluid temperature or the fluid-wall interaction strength. On the contrary, the effect of the layering at the walls clearly affects ρ_c/ρ_b. Within the range of conditions examined here, a reasonable estimate of the dependency is given by $\rho_c/\rho_b(T, \epsilon) \simeq A_\rho + B_\rho Wa\sqrt{T}$, with A_ρ and B_ρ being constant parameters. This relation enables us to formulate the following relation between the average $\bar{\rho}$ and the bulk density in the channel:
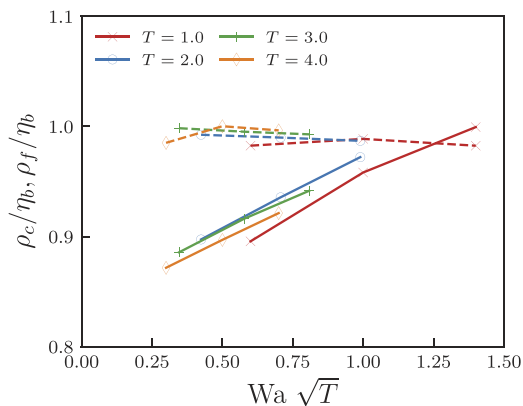
$$\bar{\rho} \simeq \rho_b \left[\frac{h - 2\delta}{h} + \frac{2\delta}{h} \left(A_\rho + B_\rho Wa\sqrt{T} \right) \right]. \qquad (20)$$

Based on our MD simulations, the fitting parameters for a LJ fluid confined between two parallel walls take the values $A_\rho \simeq 0.8$ and $B_\rho \simeq 0.1$ (Fig. 6). The approach just outlined to model the average density can be generalized to any confined fluid system and can thus present a practical tool for the design of engineering nanodevices.

D. Velocity and shear rate

A Couette flow is expected to produce a linear velocity profile for homogeneous fluids. However, the layered fluid structure near the walls causes a nonuniform mobility of the particles, resulting in undulations of the velocity profile [Fig. 7(a)].[20] The surface adsorbs a fluid layer whose thickness depends on the strength of the fluid-wall interactions. Consequently, an increase in the fluid-wall interaction strength reduces the width of the channel available for mobile particles, resulting in a higher shear rate in the bulk region of the channel [Fig. 7(b)]. In addition, the value of the shear rate evaluated at the wall depends significantly on the wall-fluid interactions, due to slip effects.[69] This phenomenon plays an important role in the study of boundary conditions and has been widely studied in the past.[37] Comparing Figs. 4(b) and 7(b), it can be noticed that the local minima in the density profile correspond to the highest shear rate. This suggests that slip occurs not only between the contact layer and the wall but that dense fluid layers also slip along each other.

E. Stress tensor

Figure 8(a) depicts the diagonal component of the stress tensor $\sigma_{yy}(y)$, including its kinetic and potential components, for a system
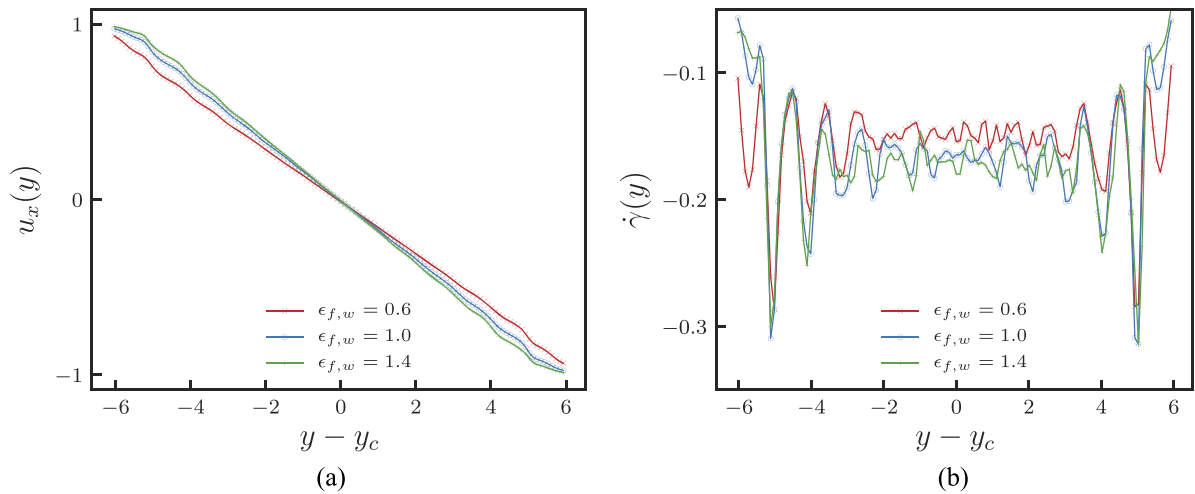

FIG. 6. Normalized average free density ρ_f/ρ_b (dashed lines) and normalized average confined density ρ_c/ρ_b (solid lines) for several temperatures' and walls' interactions.

FIG. 7. (a) Velocity and (b) shear profiles for $\epsilon_{LJ,f,w}$ = 0.6, 1.0, 1.4 at T = 1.0. Wall interactions induce deviations from the linear profile in the velocity field, giving rise to oscillations in the shear rate profile.

of temperature T = 1.0 and $\epsilon_{LJ,f,w}$ = 1.0. The kinetic and potential stress profiles oscillate in antiphase with identical amplitude such that $\sigma_{yy}(y)$ is constant, as required by the conservation of linear momentum.

Due to the planar geometry and the shear along the x direction, the only nonzero off-diagonal component of the fluid stress is given by $\sigma_{xy}(y)$. Figure 8(b) depicts kinetic, potential, and total shear stress profiles $\sigma_{xy}(y)$ for T = 1.0 and $\epsilon_{LJ,f,w}$ = 1.0. Similarly to the normal stress, the total shear stress is approximately constant since oscillations in its potential and kinetic components cancel out against each other.

Average stresses in the bulk region are easily calculated from the stress profiles. The bulk values of σ_{yy} (at $\epsilon_{LJ,f,w}$ 1.0) as a function of the temperature are shown in Fig. 8(c). Our data are complemented by normal stress values σ_{yy} obtained by Hartkamp et al.[20] at lower temperatures ($0.4 \leq T \leq 1.0$) in a system with very similar characteristics. Consistent with the equipartition theorem, the kinetic stress component is proportional to temperature as $\sigma_{yy}^{k} = -\rho_b T/m$. The larger thermal velocities at higher temperatures cause more momentum to be transferred in the normal direction by means of particle collisions. Regarding the potential stress component σ_{yy}^{v}, its dependency on the temperature is related to the nonlinear interparticles potential. At low temperatures, the attractive and repulsive interactions are approximately balanced. With the increase in temperature, the occurrence of harder collisions results in strong repulsive forces and thus more negative normal stress (or, equivalently, more positive pressure).

The bulk values of the off-diagonal stress σ_{xy} [Fig. 8(d)] show a different behavior with respect to temperature. The kinetic component again increases in absolute value as a function of the temperature. However, the MD results do not follow a linear relation and a correction factor is needed, as will be discussed in Sec. IV F 2. In contract to the normal stress, the potential shear stress component σ_{xy}^{v} decreases in absolute value, since higher thermal velocities reduce the effects of repulsive interactions between fluid layers.

F. Shear viscosity profile: Simulations and semiempirical models

Shear viscosity is evaluated as a function of the off-diagonal stress component σ_{xy} and of the shear rate, $\dot{\gamma}$, as

$$\eta(y) = \sigma_{xy}(y)\dot{\gamma}(y)^{-1}. \tag{21}$$

In analogy with the stress tensor, one can define the kinetic and potential components of the viscosity, representing the resistance to shearing flows due to particle motion and to interparticle interactions, respectively. Specifically, the kinetic component ($\propto \rho$ for homogeneous media) is predominant at low fluid densities, while the potential contribution ($\propto \rho^2$ for homogeneous media) prevails at high densities. Figures 9(a) and 9(b) show the kinetic and total shear viscosity profiles for several temperatures and wall interactions. The oscillatory behavior observed in the vicinity of the walls follows closely (but not exactly) the density profiles. Higher Wa corresponds to more pronounced layering in the viscosity profile, due to fluid adsorption at the solid interface. The viscosity in the bulk region ranges from 2.05 to 2.5, which can be explained by differences in bulk density and temperature of the systems. In the case that T = 1 and $\epsilon_{LJ,f,w}$ = 1.6, the average density in the bulk region is $\rho_b \sim 0.81$, which is approximately the same value detected in Refs. 20 and 36. Thus, under such circumstances, it is possible to compare the value of the viscosity in the bulk region against previous work. From our simulation, we observe a value $\eta_b \sim 2.18$, which is consistent with the values $\eta_b \sim 2.06$ obtained in Ref. 20 and $\eta_b \sim 2.15$ found in Ref. 36.

Analytical expressions to model the viscosity of dense inhomogeneous real fluids are not available up to date. However, for simple hard sphere (HS) systems, Din and Michaelides[18] proposed
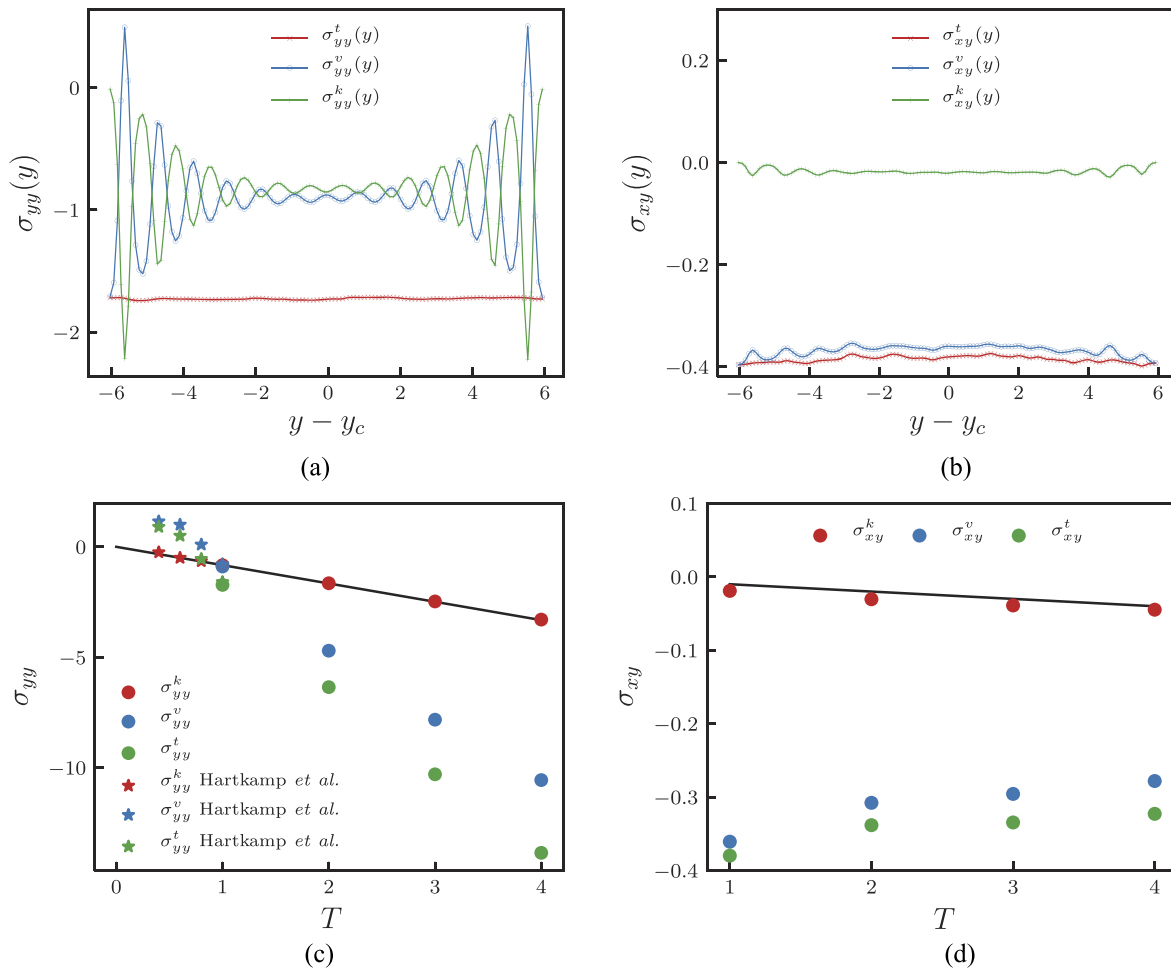
FIG. 8. (a) Stress tensor diagonal component σ_{yy}^t and (b) off-diagonal component σ_{xy}^t, evaluated for $T = 1.0$ and $\epsilon_{LJ,f,w} = 1.0$. Bulk values of the diagonal component σ_{yy}^t (c) and of the off-diagonal component σ_{xy}^t (d) of the stress tensor evaluated at different temperatures for $\epsilon_{LJ,f,w} = 1.0$. Additional data from Hartkamp et al.[20] are reported for $T < 1$. The linear dependence between the kinetic contribution and the temperature is highlighted by the black line.

a theoretical framework that allows us to derive the viscosity profile directly from the Boltzmann equation (for more details, see Appendix D). In what follows, such a framework is briefly introduced and, by means of proper empirical correction factors directly obtained from our simulations, it is employed to model the viscosity of LJ fluids. The main aim of the remaining part of this section is to obtain a widely applicable functional relation between viscosity and density profiles, which enables us to accurately determine the complex behavior of this transport property in confined fluids.

1. Analytical model for the viscosity of inhomogeneous hard-sphere fluids

The theoretical derivation proposed by Din and Michaelides[18] also distinguishes between the kinetic and the potential contributions to the fluid viscosity. The kinetic component is a local function

of the density that can be written as

$$\eta_{HS}^k(y) = \frac{16}{5}\eta^0 \rho(y) b^*(y), \tag{22}$$

where $\eta^0 = 5(k_B Tm/\pi)^{1/2}/(16\sigma_{HS}^2)$ is the zero-density viscosity and $b^*(y)$ is a dimensionless space-dependent function that can be evaluated by solving the following integral equation:

$$4b^*(y) \int_{-\sigma_{HS}}^{\sigma_{HS}} g(y, y + y')\rho(y + y') dy'$$
$$- \frac{25}{3} \int_{-\sigma_{HS}}^{\sigma_{HS}} [b^*(y + y') - b^*(y)] g(y, y + y')\rho(y + y') dy'$$
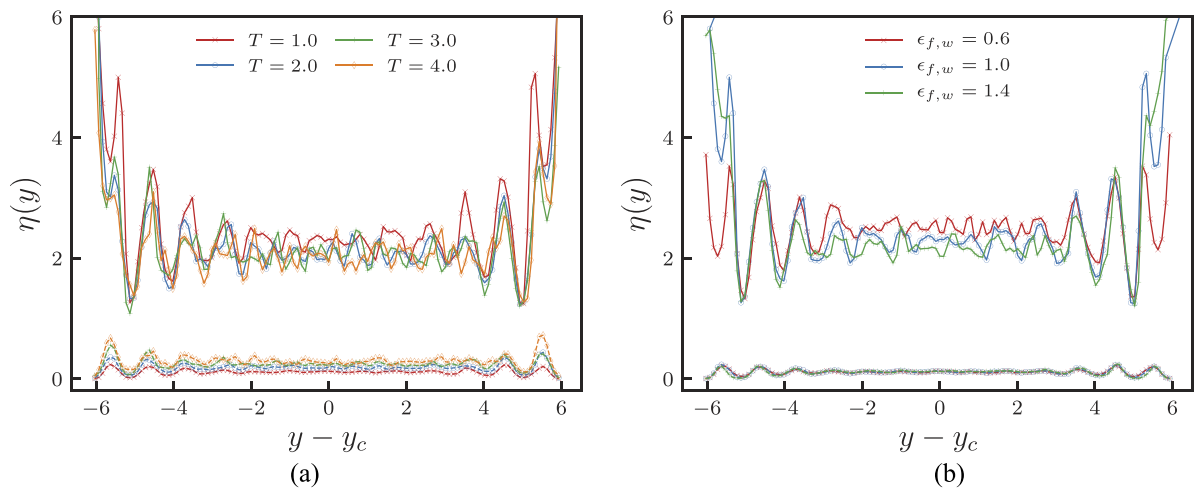$$= \frac{5}{2} + \frac{\pi}{3} \int_{-\sigma_{HS}}^{\sigma_{HS}} g(y, y + y')\rho(y + y') dy'. \tag{23}$$

FIG. 9. Solid lines represent the total shear viscosity profile (a) at different temperatures $1.0 \leq T \leq 4.0$ for $\epsilon_{LJ,f,w} = 1.0$ and (b) at various wall interaction potentials, i.e., $\epsilon_{LJ,f,w} = 0.6, 1.0, 1.4$ and $T = 1$. The kinetic component of the viscosity in both (a) and (b) is displayed as dashed lines.

The potential contribution to the viscosity for a HS fluid is given by a nonlocal expression of density

$$\eta_{HS}^{v}(y) = \frac{8\pi}{5}\eta^0 \int_{-\sigma_{HS}}^{\sigma_{HS}} y' \sin^3\left(\arccos(y')\right) I(y, y')\, dy', \quad (24)$$

where $I(y, y')$ indicates the following infinite series:

$$I(y, y') = y' \sum_{s=1}^{\infty} \frac{(-y'^{s-1})}{s!} \frac{\partial^{s-1}}{\partial^{s-1} y}$$
$$\times \left\{ g(y, y + y')\rho(y)\rho(y + y')\left[2 + b^*(y + y') + b^*(y)\right] \right\}, \quad (25)$$

where g denotes the pair correlation function.

Among the possible approximations of the pair correlation function of the inhomogeneous fluid, $g(y, y + y')$, the one proposed by Fischer and Methfessel[70] is adopted here. These authors approximated $g(y, y + y')$ as the radial correlation function of a homogeneous fluid evaluated at an average density $\bar{\rho}(y, y + y')$, namely,

$$g(y, y + y') = g^{hom}\left[r = \sigma_{HS}, \bar{\rho}(y, y + y')\right], \quad (26)$$

where $\bar{\rho}(y, y + y')$ is the density average over a sphere centered in $y + \frac{y'}{2}$, with radius $\sigma_{HS}/2$, i.e.,

$$\bar{\rho}(y, y + y') = \frac{6}{\pi\sigma_{HS}^3} \int_{\mathbf{r} < \frac{\sigma_{HS}}{2}} \rho\left(y + \frac{y'}{2} + \mathbf{r}\right) d\mathbf{r}. \quad (27)$$

Moreover, if the Carnahan-Starling equation of the state is adopted,[71] then the radial correlation function of a homogeneous fluid can be computed as $g^{hom}[r = \sigma_{HS}, \bar{\rho}] = (1 - 0.5\xi)/(1 - \xi)^3$, with $\xi = \pi\sigma_{HS}^3\bar{\rho}/6$. It is clear from Eqs. (24) and (25) that, in general, the potential contribution to the viscosity, unlike the

kinetic one, cannot be expressed as a local function of the density or its derivatives. However, the effect of nonlocality may be neglected under certain system conditions, as will be shown in Sec. F.4.

2. Shear viscosity of bulk fluid: From hard-sphere to Lennard-Jones

When using kinetic theory to model a fluid characterized by a complex interaction potential, such as LJ, the temperature dependency of the viscosity is often not accounted properly. To overcome this issue, an empirical correction factor $c_\eta^k(T)$ is introduced,[35,72] obtained by comparing the viscosity in the bulk region computed from MD simulations with the HS viscosity given by Eqs. (22)–(24). Consequently, the kinetic viscosity in the bulk can be described by the following expression:

$$\eta^k \sim c_\eta^k(T)\, \eta_{HS}^k. \quad (28)$$

The correction parameter is found to be $c_\eta^k(T) \sim 1/\Omega(T)$, where Ω is a factor introduced by Chapman and Enskog to obtain the viscosity of a LJ dilute gas with kinetic theory. The value of $\Omega(T)$ is difficult to compute directly and is therefore typically either reported in tables[73] or provided in the form of empirical expressions.[74] Here, $\Omega(T)$ is evaluated according to the expression obtained by Neufeld,[74]

$$\Omega(T) = \frac{A_\Omega}{T^{B_\Omega}} + \frac{C_\Omega}{e^{D_\Omega T}} + \frac{D_\Omega}{e^{F_\Omega T}} + R_\Omega T^B \sin(S_\Omega T_\Omega^W - P_\Omega), \quad (29)$$

with A_Ω, B_Ω, C_Ω, D_Ω, E_Ω, F_Ω, R_Ω, S_Ω, W_Ω, and P_Ω being fitting parameters. The potential contribution to the viscosity strongly depends on the interactions between the particles. In the case of LJ systems, the potential viscosity exhibits an Arrhenius-like dependence on temperature[72] that is not captured by the HS model. Thus, we propose to correct the HS potential viscosity in the bulk region as

$$\eta^v \sim c_\eta^v(T)\,\eta_{\text{HS}}^v, \tag{30}$$

where $c_\eta^v(T)$ is a correction factor. By fitting the ratio $\eta^v/\eta_{\text{HS}}^v$ computed with our MD simulations, we have found that this correction factor is well approximated by the empirical relation $c_\eta^v(T) = C_\eta e^{D_\eta/T}$, with $C_\eta = 0.35$ and $D_\eta = 1.2$ being fitting parameters. Figure 10 shows a comparison between the correction factors $c_\eta^v(T)$ [$c_\eta^k(T)$] and the ratio $\eta^v/\eta_{\text{HS}}^v$ ($\eta^k/\eta_{\text{HS}}^k$) evaluated with MD. The correction factors are able to approximate the values predicted by MD with an accuracy lower than the standard error for almost any value of the temperature considered here. Finally, as implicitly assumed also in Ref. 18, the HS diameter σ_{HS} is considered approximately equivalent to the LJ parameter σ_{LJ}.

3. Nonlocal density-viscosity relation

If we consider only the zeroth-order terms of Eq. (25), the following approximate expression for the viscosity is obtained:

$$\eta(y) = \frac{16\eta^0}{5\Omega}\rho(y)b^*(y) + \frac{8\pi c_\eta^v \eta^0}{5}\rho(y)\int_{-\sigma_{\text{LJ}}}^{\sigma_{\text{LJ}}} K(y,y')\,dy', \tag{31}$$

where $K(y,y')$ is a kernel function responsible for the nonlocal contributions to the potential component

$$K(y,y') = y'^2\sin^3\!\big(\arccos(y')\big)g(y,y+y')\rho(y+y')$$
$$\times\big[2 + b^*(y+y') + b^*(y)\big]. \tag{32}$$

Equation (31) represents a semiempirical nonlocal viscosity model, consistent with the kinetic theory and similar in form to local average density models presented in previous works.[21,35,75] In this work, we compare our model with the one by Hoang and Galliero,[21] showing that the latter is inappropriate for strongly layered fluids. Specifically, by fitting numerous MD simulation data, Hoang and Galliero[21] proposed the following empirical nonlocal model for the viscosity in a narrow channel:

$$\eta(y) = \frac{\eta^0}{\Omega}\left(\frac{\rho(y)}{\rho_b}\right)^\gamma + \eta_{corr}\big[T(y),\rho_{\text{eff}}(y)\big], \tag{33}$$

where $\gamma = 0.8e^{0.022T^2}/\rho_b$ and $\rho_{\text{eff}}(y) = \int\omega(|y-y'|)\rho(y')dy'$ is a nonlocal average density with kernel $\omega(y)$ given by

$$\omega(y) = \begin{cases} \dfrac{6}{\sigma_{\text{LJ}}^3}\left[\left(\dfrac{\sigma_{\text{LJ}}}{2}\right)^2 - y^2\right] & \text{if } y \le \dfrac{\sigma_{\text{LJ}}}{2} \\[4pt] 0 & \text{otherwise.}\end{cases} \tag{34}$$

Furthermore, $\eta_{corr}[T,\rho_{\text{eff}}(y)]$ in Eq. (33) takes the following functional expression:

$$\eta_{corr}[T,\rho_{\text{eff}}(y)] = b_1\big(e^{b_2\rho_{\text{eff}}} - 1\big) + b_3\big(e^{b_4\rho_{\text{eff}}} - 1\big) + \frac{b_5}{T^2}\big(e^{b_6\rho_{\text{eff}}} - 1\big), \tag{35}$$

with fitting coefficients b_i given in the study of Galliéro et al.[76]

4. Local density-viscosity models

The complexity of the previously proposed nonlocal viscosity model can limit its practicality, for example, when limited computational resources are available. Here, we make three assumptions to simplify the model and obtain purely local expressions, which do not require the computation of space convolutions. First, the pair correlation function in the confined region is assumed to not differ significantly from its bulk counterpart, namely, $g(y,y+y') \sim g_b(\sigma_{\text{LJ}})$. Second, $b^*(y)$ is assumed to be approximately constant between $y - \sigma_{\text{LJ}}$ and $y + \sigma_{\text{LJ}}$, i.e., $b^*(y+y') \sim b^*(y)$ in Eq. (32). Finally, we assume that the value of the integral $\int_{-\sigma_{\text{LJ}}}^{\sigma_{\text{LJ}}}\sin^3\big(\arccos(y')\big)\rho(y+y')\,dy'$ is only weakly dependent on y. Consequently, Eq. (31) simplifies to

$$\eta(y) \simeq \frac{\rho(y)}{\rho_b}\left[\frac{b^*(y)}{b_b^*}\eta_b^k + \frac{1+b^*(y)}{1+b_b^*}\eta_b^v\right], \tag{36}$$

where η_b, ρ_b, and b_b^* are shear viscosity, density, and $b^*(y)$ evaluated in the bulk, respectively. Equation (36) provides a local functional expression relating shear viscosity to the density variations at the fluid-solid interface. The analysis of our MD results shows that the ratio $b^*(y)/b_b^*$ mainly depends on the wall interaction and not on the temperature. The profile of $b^*(y)$ as a function of the wall interaction strength is shown in Fig. 11. By analyzing the MD data, we
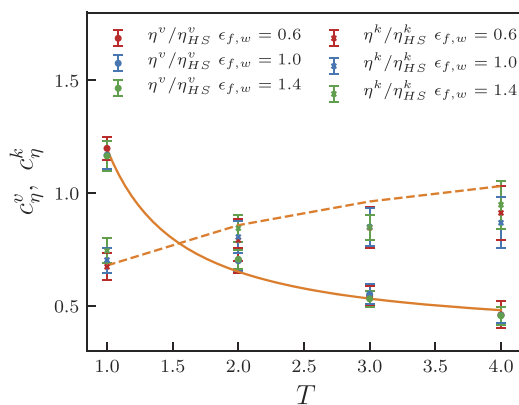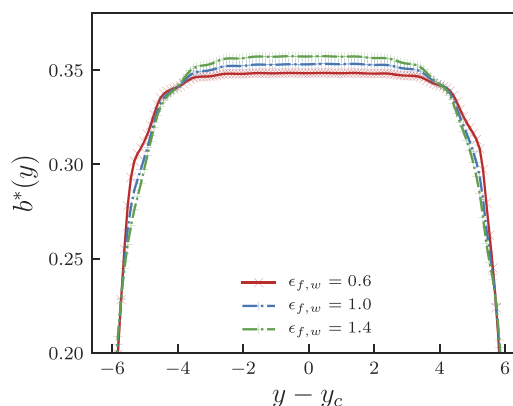
FIG. 10. Correction factors $c_\eta^v(T)$ (solid line) and $c_\eta^k(T)$ (dashed line) for the bulk values of potential and kinetic viscosity. The correction factors are compared with the ratios η/η_{HS} computed directly from our MD results. The error bars indicate standard errors computed from the distribution of viscosity values inside the bulk region.

FIG. 11. Function $b^*(y)$ computed from MD density profiles through Eq. (23) for different wall interaction potentials, i.e., $\epsilon_{\text{LJ},f,w} = 0.6$ (red solid line), $\epsilon_{\text{LJ},f,w} = 1.0$ (blue dashed line), and $\epsilon_{\text{LJ},f,w} = 1.4$ (green dashed line), at $T = 1$. Evidently, for stronger wall interactions, $b^*(y)$ has higher bulk values and shows a slower decay at the wall interface.

found that the ratio $b^*(y)/b_b^*$ can be well approximated without using Eq. (23), by fitting the following empirical expression to MD simulation results:

$$\frac{b^*(y)}{b_b^*} \simeq 1 - A_b\, e^{B_b(y-y_w)/\epsilon_{\mathrm{LJ},f,w}^{C_b}}, \qquad (37)$$

where $y - y_w$ is the distance from the wall and the fitting coefficients take the value $A_b = 0.59$, $B_b = 1.61$, and $C_b = 0.15$. Equation (37) can be used to obtain a straightforward evaluation of $b^*(y)$, given that its bulk value b_b^* can be computed from Eq. (23) as

$$b_b^* = \frac{\pi}{12} + \frac{5}{16\,\sigma_{\mathrm{LJ}}\,\rho_b\,g^{hom}[r = \sigma_{\mathrm{LJ}}, \rho_b]}. \qquad (38)$$

Assuming that $b^*(y) \sim b_b^*$, Eq. (36) reduces to the linear relation

$$\eta(y) \sim \frac{\eta_b}{\rho_b}\,\rho(y), \qquad (39)$$

observed also by Morciano *et al.*[36] by analyzing MD data correlations at a fixed temperature $T = 1$. Interestingly, Fig. 12(a) shows that the linear relation in Eq. (39) can be directly detected from MD results and holds for any analyzed temperature. Figure 12(b) shows that the corresponding standard error associated with this linear model ranges between 15% and 30% if the first fluid layer in contact with the walls is included and between 5% and 15% if the first fluid layer at the walls is excluded. Equation (39) provides an attractive approximation as it does not require computing the convolution kernel or $b^*(y)$, but its applicability is limited to moderate fluid-wall interaction (low Wa) or to situations in which the first fluid layer in contact with the walls is excluded.
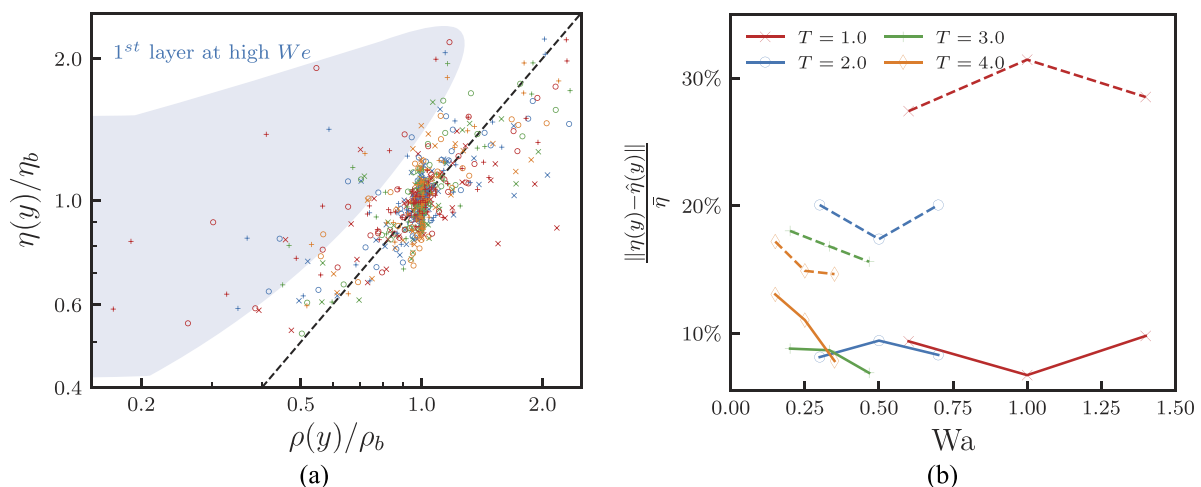
5. Comparison between the different models

In Fig. 13, we compare the performance of the proposed viscosity models in predicting MD results for system conditions $\epsilon_{\mathrm{LJ},f,w}$ = 0.6 [(a) and (b)], $\epsilon_{\mathrm{LJ},f,w}$ = 1.0 [(c) and (d)], and $\epsilon_{\mathrm{LJ},f,w}$ = 1.4 [(e) and (f)] at temperatures $T = 1.0$ [(a), (c), and (e)] and $T = 4.0$ [(b), (d), and (f)]. We also report the viscosity profile predicted by the model introduced by Hoang and Galliero[21] and given by Eq. (33). Regarding the bulk region, the qualitative features of the shear viscosity are well predicted both by our model (discussed in Sec. IV F 2) and by the empirical formula of Ref. 76. On the contrary, for the inhomogeneous region in proximity of the walls, two regimes may be distinguished. At Wa $\ll 1$, a weaker layering is observed in the viscosity profile and the nonlocal effects are negligible. In this regime, both our local models and Hoang's model,[21] which is based on a correlation derived for uniform fluids, are able to accurately reproduce MD results. However, when the Wall number increases, i.e., Wa $\simeq 1$, the effects of the walls become increasingly more important, and Hoang's model fails to predict the viscosity profile. The models proposed in this work, including the local ones, show good agreement with MD results, even in the case of Wa $\simeq 1$. As expected from the derivation, the nonlocal model outperforms the local ones. Furthermore, when looking at the first fluid layer in contact with the walls, the linear model of Eq. (36) is more accurate than the simplified linear model in Eq. (39).

6. Darcy-Weisbach friction factor in nanopipes

The findings of this work can be applied to study, for instance, the Darcy-Weisbach friction factor in nanogeometries. As extensively discussed in the work of Liakopoulos *et al.*,[77] it is possible to use a modification of the Darcy-Weisbach friction factor to model flows in nanoscale confined geometries. For an infinitely wide channel with height h, the Darcy-Weisbach friction factor, f, is given
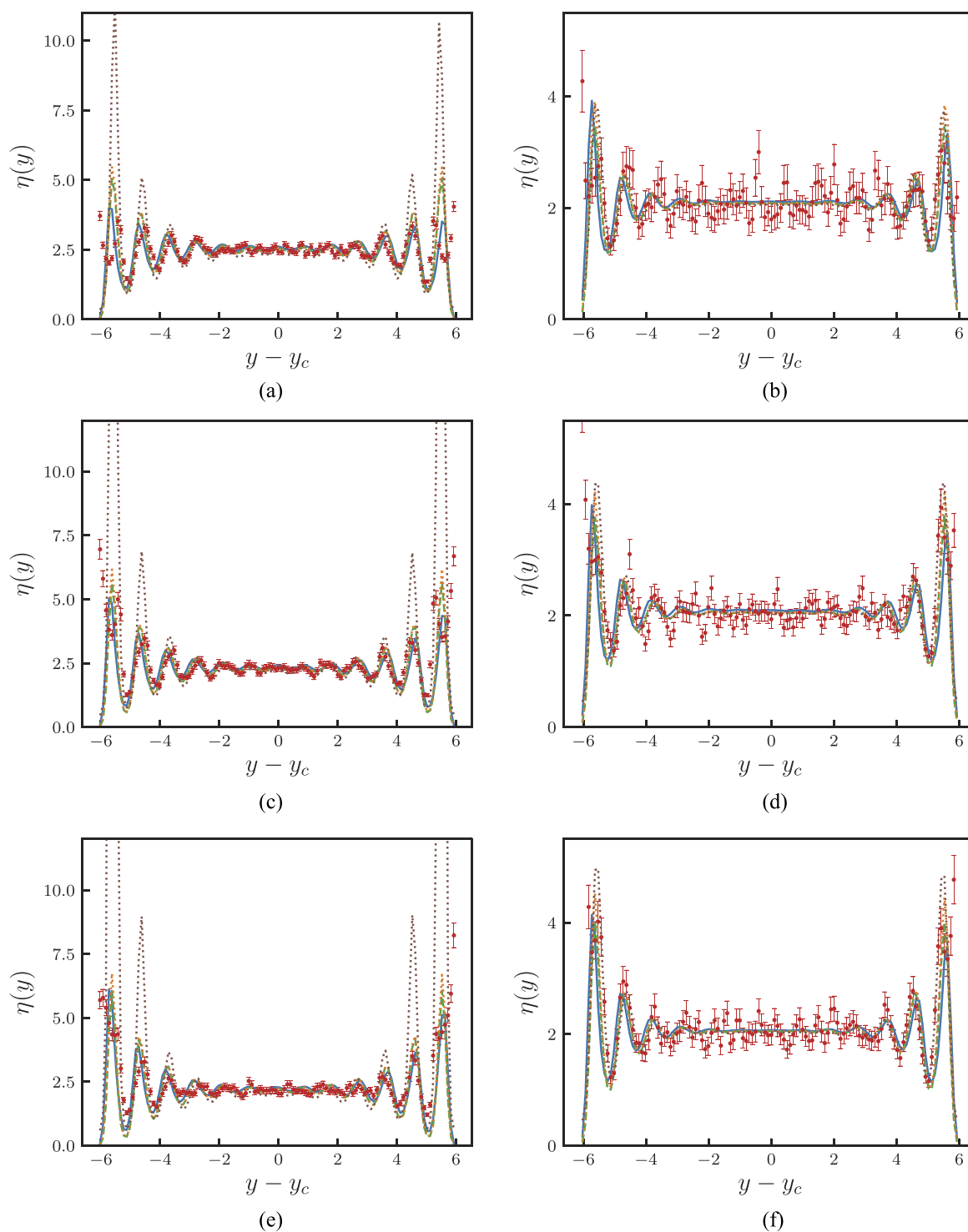

FIG. 12. (a) Normalized viscosity against normalized density profiles for liquid-solid interfaces obtained by MD (symbols) and by Eq. (39) (black dashed line). The symbols correspond to different wall potentials ($\times$: $\epsilon_{\mathrm{LJ},f,w}$ = 0.6; $\circ$: $\epsilon_{\mathrm{LJ},f,w}$ = 1.0; and +: $\epsilon_{\mathrm{LJ},f,w}$ = 1.4), whereas distinct colors are used to map the temperatures (red, blue, green, and orange indicate $T = 1.0$, $T = 2.0$, $T = 3.0$, and $T = 4.0$, respectively). The points inside the shaded blue area correspond to the viscosity and density of the first fluid layer in contact with the walls for systems at high Wa. (b) Root mean square error normalized with respect to the average channel viscosity when employing Eq. (39) to model the viscosity of the whole system (dotted lines) and of the system without the first fluid layer at the walls (solid lines).

FIG. 13. Shear viscosity profile for $\epsilon_{\mathrm{LJ},f,w}$ = 0.6 [(a) and (b)], $\epsilon_{\mathrm{LJ},f,w}$ = 1.0 [(c) and (d)], and $\epsilon_{\mathrm{LJ},f,w}$ = 1.4 [(e) and (f)] at temperatures T = 1.0 [(a), (c), and (e)] and T = 4.0 [(b), (d), and (f)]. MD results (red dots) are compared against the nonlocal model given by Eq. (31) (blue solid line), the linear model of Eq. (36) (green dashed line), the simplified linear model in Eq. (39) (orange dotted line), and, finally, the model proposed by Hoang and Galliero[21] [Eq. (33)]. The bars reported for MD results show the standard errors computed assuming that every point has the same relative error of the viscosity in the bulk region.

by

$$f = \frac{-2D\dfrac{\partial p}{\partial x}}{\bar{\rho}\bar{V}^2}, \tag{40}$$

with p being the pressure, $D = 2h$ being the hydraulic diameter, and $\bar{\rho} = \frac{1}{h}\int_0^h \rho(y)$ and $\bar{V} = \frac{1}{h}\int_0^h u_x(y)$ being the average density and velocity in the cross section, respectively. From momentum conservation, assuming a Poiseuille flow, the local velocity can be computed by solving the following differential equation:

$$\frac{d}{dy}\left(\eta(y)\frac{du_x(y)}{dy}\right) = \frac{\partial p}{\partial x}. \tag{41}$$

For symmetric flows, Eq. (41) has the solution

$$u_x(y) = \frac{\partial p}{\partial x}\int_0^y \frac{y'}{\eta(y')}dy' + u_s, \tag{42}$$

where $u_s = u_x|_{y=0}$ is the slip velocity at the wall. The integrals in Eq. (42) can be solved by using one of our (local or nonlocal) models to approximate $\eta(y)$. For simplicity, here we will use the local model in Eq. (39), equipped with the density profile approximation in Eq. (14). After some algebraic manipulations, we obtain the following expression for the Darcy-Weisbach friction factor in nanochannels:

$$f = \frac{-2D\dfrac{\partial p}{\partial x}}{\dfrac{\rho_b}{h}\int_0^h\left(1 + Ae^{-By}\cos\frac{2\pi y}{l}\right)dy\left[\dfrac{1}{h\eta_b}\dfrac{\partial p}{\partial x}\int_0^h\int_0^y y'\left(1 + Ae^{-By'}\cos\frac{2\pi y'}{l}\right)^{-1}dy'dy + u_s\right]^2}. \tag{43}$$

The more accurate nonlocal viscosity model in Eq. (31) can also be employed, but this would increase the computational cost. Moreover, this approach can be generalized to study the nanochannel with arbitrary shapes.

G. Global shear viscosity for a fluid in a confined geometry

Following the same approach as in Sec. IV C, we define the confined viscosity $\eta_c = \frac{1}{V_c}\int_{V_c}\eta(y)dV$ and the free viscosity $\eta_f = \frac{1}{V_f}\int_{V_f}\eta(y)dV$. With prior knowledge of η_c and η_f, the average viscosity of the system in the channel $\bar{\eta}$ can then be expressed as

$$\bar{\eta} = \eta_b\left(\frac{V_f}{V_{tot}}\frac{\eta_f}{\eta_b} + \frac{V_c}{V_{tot}}\frac{\eta_c}{\eta_b}\right), \tag{44}$$
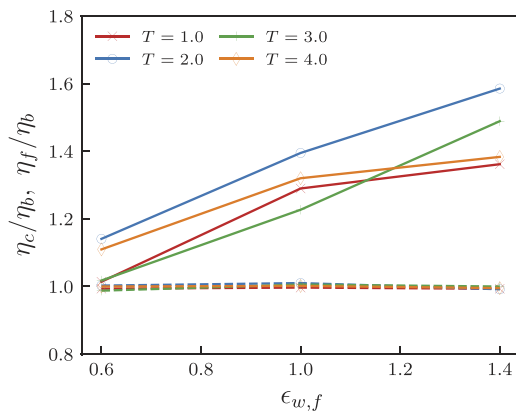

FIG. 14. Free viscosity (dashed lines) and confined viscosity (solid lines) normalized with respect to the viscosity in the bulk region.

where the boundary of the confinement region is defined through δ. This expression can then be parameterized with the variations of η_c and η_f as a function of the temperature and the fluid-wall interaction. Figure 14 shows that the free viscosity can be considered approximately equal to the viscosity in the bulk region, regardless of the fluid temperature and the fluid-wall interaction strength. Conversely, the ratio η_c/η_b is linearly dependent on $\epsilon_{LJ,f,w}$ and independent of T. Based on these observations, Eq. (44) is rewritten as

$$\bar{\eta} \sim \eta_b\left[\frac{h-2\delta}{h} + \frac{2\delta}{h}\left(A_\eta + B_\eta\,\epsilon_{LJ,f,w}\right)\right], \tag{45}$$

with A_η and B_η being some fitting parameters. The values $A_\eta \sim 1.3$ and $B_\eta \sim 0.5$ yield agreement of Eq. (45) and MD results within 10%. Equation (45) allows us to predict the average viscosity in a channel based on its geometry (through h), on the fluid-wall coupling thermodynamic parameter δ, and on the bulk fluid viscosity, which can be accurately modeled through the equation of state for homogeneous fluids (i.e., as in Sec. IV F 2 or as in Ref. 34).

V. SUMMARY AND CONCLUSIONS

We have performed extensive MD simulations of a nanoconfined LJ fluid with the purpose of, (1) scrutinizing the effects of temperature and fluid-wall interactions on the inhomogeneous interfacial fluid structure and, (2) deriving and validating macroscopic relations capable of modeling inhomogeneous transport properties. The MD simulations are complemented by analyses of the different kernels adopted in the simulations and the pertinent physical properties, including density, momentum, stress tensor, shear rate, and viscosity.

Close to the wall, layering of fluid particles results in oscillations in both density and shear rate profile. These oscillations are enhanced for strongly attractive walls and low temperatures.

Following the work of Chiavazzo et al.,[66] we adopted the average energy of fluid atoms due to the presence of the wall to distinguish between a region of width δ, the "confinement parameter," within which the fluid properties are directly affected by the confinement, and a region with freely moving particles. Careful analyses of the average fluid properties in these regions allow us to obtain novel ready-to-use relations, which express the average density (and viscosity) in the channel as a function of temperature, wall interaction strength, and value of density (and viscosity) in the bulk region. Such relations constitute a useful toolbox that can be readily employed in the design and the analysis of nanofluidic devices where solid-fluid interfaces play an important role.

Furthermore, we have investigated how the fluid confinement affects the local and average shear viscosity, which is crucial for both tribological applications and nanofluidics. The shear viscosity profile was evaluated from MD simulations and compared against multiple theoretical frameworks and models.

In particular, the theoretical framework derived by Din and Michaelides[18] for a hard sphere fluid was adapted to model the viscosity profile of inhomogeneous dense LJ fluids as a function of the density profile, system temperature, and wall interactions. Specifically, we proposed an accurate and robust nonlocal model for the viscosity, exhibiting a convolution structure, Eq. (31), which, under certain approximations, can be reduced to a local linear model (in terms of density), Eq. (36), which in turn can be further simplified to the linear model in Eq. (39). These nonlocal and local models were contrasted against both MD simulations and a model proposed by Hoang and Galliero[21] over a wide range of interfacial conditions and temperatures.

At a small Wall number, Wa ≪ 1, layering is weak and nonlocal effects are negligible. In this regime, both our models and the model proposed by Hoang and Galliero[21] can accurately reproduce MD results. At Wa ~ 1, the model of Hoang and Galliero[21] failed to predict the viscosity profile, whereas our models showed good agreement with MD results. In all cases, the nonlocal model in Eq. (31)

performed better than the local one. Furthermore, the linear model of Eq. (36) exhibited higher accuracy compared with the simplified linear model in Eq. (39).

The functional relations developed here can be implemented in numerical methods dealing with mesoscopic fluid flows (e.g., Ref. 78) to improve the accuracy of such methods in the description of fluid-solid interfaces. But also in models in the framework of dynamic density-functional theory (e.g., Refs. 22–24), which suffer from unresolved closures, such as the dependence of viscosity on density. Moreover, since the functional relations are derived from a general theoretical framework for HS systems, they can be employed to model the inhomogeneous properties of non-LJ fluids by appropriately adjusting the empirical factors. Of particular interest would also be liquid-vapor interfaces in confinement, where the treatment of the stress tensor and emergence of surface tension should be crucial (e.g., Ref. 79).

APPENDIX A: STRAIN RATE AND THERMOSTATS

Some of the most frequently used thermostats in MD are the Langevin,[80] Nosé-Hoover (NH),[46–48] and dissipative particle dynamics[81] thermostats. In this work, a NH thermostat is adopted, which has been shown to perform well for weakly sheared systems,
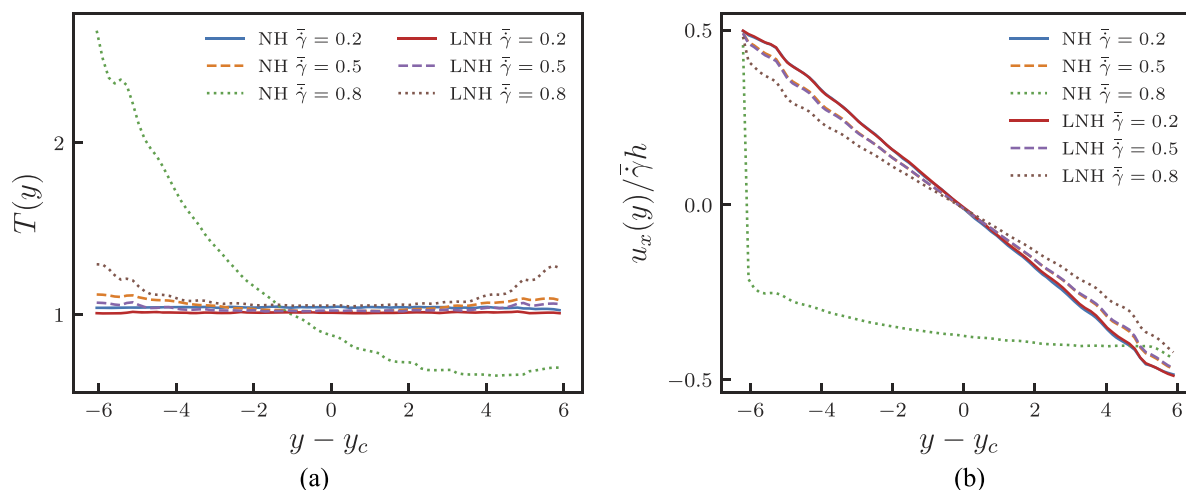

FIG. 15. (a) Temperature profiles for different average shear rates $\bar{\dot{\gamma}}$, obtained using a single global NH thermostat and a series of LNH thermostats, each controlling a region of (nondimensional) unitary width, at fixed temperature $T = 1.0$. (b) Velocity profiles normalized with respect to h and $\bar{\dot{\gamma}}$ induced by the moving walls for different shear rates, at fixed temperature $T = 1.0$.

and, unlike the Langevin and dissipative particle dynamics thermostats, does not alter the value of the system's viscosity.[45] However, NH is a global thermostat and consequently may suffer from the inhomogeneity of the system, since the heat is not generated uniformly across the domain. To overcome this limitation, a series of local Nosé-Hoover (LNH) thermostats is used, each (nondimensional) unitary width. A similar strategy was adopted in other works, e.g., Ref. 20. To avoid biasing the fluid flow, the LNH thermostats are applied only in the directions perpendicular to the flow, i.e., in the y and z directions, and the relaxation time adopted is $\tau = 1.0$, in line with the discussion in Ref. 82.

Figures 15(a) and 15(b) compare temperature and velocity profiles obtained with NH and LNH thermostats for different shear rates. Figures 15(a) and 15(b) clearly show that the global thermostat is unable to keep a flat temperature in proximity of the walls, where the local shear rate tends to reach higher values.

APPENDIX B: BULK DENSITIES

For completeness, in Fig. 16, we report the values of bulk densities and bulk shear viscosities for the analyzed systems as a function of the wall number. At a given T, a higher $\epsilon_{f,w}$ corresponds to lower ρ_b and η_b since more particles are adsorbed at the walls. A more complex behavior is observed if $\epsilon_{f,w}$ is fixed: for hydrophobic walls ($\epsilon_{f,w} = 0.6$), both ρ_b and η_b increase as a function of T. For neutral walls ($\epsilon_{f,w} = 1.0$), ρ_b is roughly independent of T, while η_b tends to increase with temperature. For hydrophilic walls ($\epsilon_{f,w} = 1.4$), ρ_b tends to decrease with T, while η_b is about constant. As a result, higher temperatures in a nanochannel tend to hinder adsorbed particles at walls for a hydrophobic substrates and to enhance them for a hydrophilic one.

APPENDIX C: RHEOLOGICAL EFFECTS

Non-Newtonian effects manifest at high shear rates, with the onset shear rate depending on the state point of the fluid. For example, for a dense homogeneous LJ fluid ($\rho = 0.84$, $T = 1.0$), shear-thinning is observed at shear rates above approximately 0.1.[83] Other rheological phenomena, such as normal stress differences, have been shown to be very small for shear rates up to 0.5 for a homogeneous fluid near the LJ triple point ($\rho = 0.8442$, $T = 0.72$).[38] In Fig. 17, we report the average shear stress in our confined sheared system against the average shear rate for the most critical case ($T = 1.0$ and $\epsilon_{f,w} = 0.6$). No significant rheological effects are evidenced for shear rates below 0.2. Therefore, we adopt $\bar{\dot{\gamma}} \sim 0.15$ in order to have a high signal-to-noise ratio, while remaining in the Newtonian regime.

APPENDIX D: DERIVATION OF THE VISCOSITY OF A DENSE INHOMOGENEOUS HARD-SPHERE FLUID FROM KINETIC THEORY

For dense inhomogeneous hard sphere systems, Din and Michaelides[18] derived an expression for the shear viscosity directly from the Boltzmann equation. The main steps of the derivation are outlined here, and the interested reader is referred to the original paper for more details.

The starting point is the revised Enskog equation for the singlet probability density function $W_1(\mathbf{r}_1, \mathbf{u}_1, t)$ of inhomogeneous dense fluid[84]

$$
\begin{aligned}
\frac{\partial W_1}{\partial t} &+ \frac{\partial W_1}{\partial \mathbf{r}_1} \mathbf{u}_1 + \frac{\partial W_1}{\partial \mathbf{u}_1} \dot{\mathbf{u}}_1 \\
&= \iint_{\mathbf{k} \cdot \mathbf{u}_{21} > 0} \bigg[g(\mathbf{r}_1, \mathbf{r}_1 + \sigma_{HS}\mathbf{k}) W_1(\mathbf{r}_1, \mathbf{u}_1', t) \\
&\quad \times W_1(\mathbf{r}_1 + \sigma_{HS}\mathbf{k}, \mathbf{u}_2', t) - g(\mathbf{r}_1, \mathbf{r}_1 - \sigma_{HS}\mathbf{k}) W_1(\mathbf{r}_1, \mathbf{u}_1, t) \\
&\quad \times W_1(\mathbf{r}_1 - \sigma_{HS}\mathbf{k}, \mathbf{u}_2, t) \bigg] \sigma_{HS}^2 (\mathbf{k} \cdot \mathbf{u}_{21}) d\mathbf{k} \, d\mathbf{u}_2,
\end{aligned} \tag{D1}
$$

where σ_{HS} is the hard sphere diameter, $\mathbf{u}_{21} = \mathbf{u}_2 - \mathbf{u}_1$ is the relative velocity between two particles, $\mathbf{k} = (\mathbf{r}_2 - \mathbf{r}_1)/|\mathbf{r}_2 - \mathbf{r}_1|$ is a unit
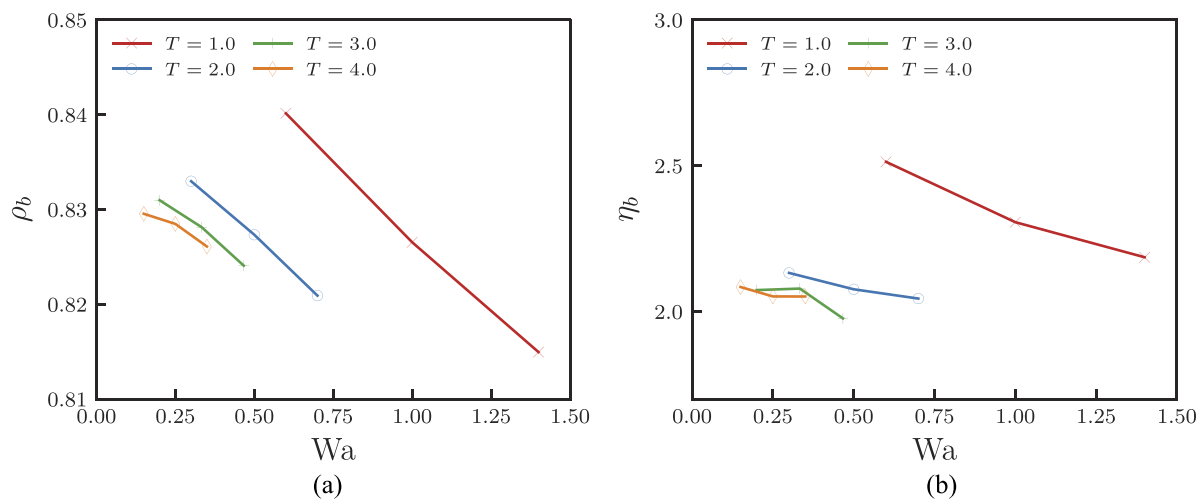

FIG. 16. Bulk values of density ρ_b (a) and viscosity η_b (b) in a nanochannel for different conditions of the system analyzed.
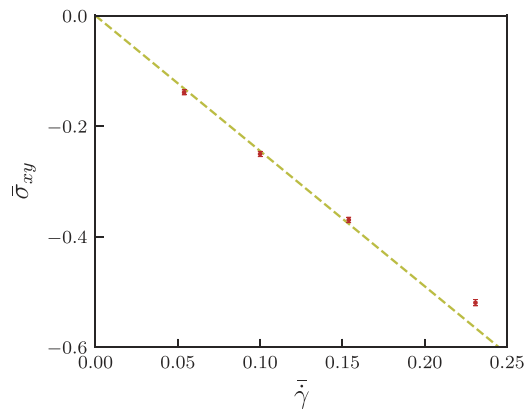
FIG. 17. Average shear stress against average shear rate is reported for the most critical scenario ($T = 1.0$ and $\epsilon_{f,w} = 0.6$). Non-Newtonian effects are evidenced at average shear rates above 0.2.

vector connecting two particles, and $\mathbf{u}_1' = \mathbf{u}_1 + (\mathbf{k} \cdot \mathbf{u}_{21})\mathbf{k}$ and $\mathbf{u}_2' = \mathbf{u}_2 - (\mathbf{k} \cdot \mathbf{u}_{21})\mathbf{k}$ are the postcollisional velocities of the two particles. In order to solve Eq. (D1) for a steady-state Couette flow, the singlet probability density function is assumed to have the following form:

$$W_1(\mathbf{r}_1, \mathbf{u}_1) = W_1^{(0)}(\mathbf{r}_1, \mathbf{u}_1 - \mathbf{u})[1 + \Phi(\mathbf{r}_1, \mathbf{u}_1 - \mathbf{u})], \qquad (D2)$$

where $W_1^{(0)}$ is the equilibrium distribution given by

$$W_1^{(0)}(\mathbf{r}_1, \mathbf{u}_1 - \mathbf{u}) = n(\mathbf{r}_1)\left(\frac{m}{2\pi k_B T}\right)^{3/2} e^{-\frac{m(\mathbf{u}_1 - \mathbf{u})^2}{2k_B T}}, \qquad (D3)$$

and $\Phi(\mathbf{r}_1, \mathbf{u}_1 - \mathbf{u})$ is a perturbation function due to nonequilibrium effects. After considerable manipulations, it turns out that the perturbation function can be expressed as a linear function of the velocity gradient, namely,

$$\Phi(\mathbf{r}_1, \mathbf{u}_1 - \mathbf{u}) = -b(\mathbf{r}_1)\left(\frac{m}{2k_B T}\right)$$
$$\times \left[(\mathbf{u}_1 - \mathbf{u})(\mathbf{u}_1 - \mathbf{u}) - |\mathbf{u}_1 - \mathbf{u}|^2\, 1/3\right] : \nabla_{\mathbf{r}_1}\mathbf{u}, \qquad (D4)$$

where $b(\mathbf{r}_1)$ is a space-dependent function, which is nondimensionalized as $b^*(y) = \sqrt{\pi k_B T/4\, m\sigma_{HS}^2}\, b(y)$. This function can then be evaluated by solving numerically the following integral equation:

$$4b^*(y)\int_{-\sigma_{HS}}^{\sigma_{HS}} g(y, y + y')\rho(y + y')dy'$$
$$- \frac{25}{3}\int_{-\sigma_{HS}}^{\sigma_{HS}}\left[b^*(y + y') - b^*(y)\right]g(y, y + y')\rho(y + y')dy'$$
$$= \frac{5}{2} + \frac{\pi}{3}\int_{-\sigma_{HS}}^{\sigma_{HS}} g(y, y + y')\rho(y + y')dy', \qquad (D5)$$

derived combining Eqs. (D1)–(D4).

Hence, it is possible to determine the rate of change of the ensemble averaged quantity $m\mathbf{u}_1$ as

$$\frac{\partial}{\partial t}\langle nm\mathbf{u}_1\rangle + \nabla_{\mathbf{r}_1} \cdot \langle nm\mathbf{u}_1 \otimes \mathbf{u}_1\rangle - \frac{\mathbf{F}}{m} \cdot \left\langle n\frac{\partial(m\mathbf{u}_1)}{\partial \mathbf{u}_1}\right\rangle = -\nabla_{\mathbf{r}_1} \cdot \theta(m\mathbf{u}_1), \qquad (D6)$$

where the brackets indicate

$$\langle \rangle = \int_{-\infty}^{+\infty} d\mathbf{u}_1\, W_1(\mathbf{r}_1, \mathbf{u}_1) \qquad (D7)$$

and $\theta(m\mathbf{u}_1)$ denotes the collision contribution given by

$$\theta(m\mathbf{u}_1) = -\frac{1}{2}\sigma_{HS}^3 \iiint_{\mathbf{k} \cdot \mathbf{u}_{21} > 0} m(\mathbf{u}_1' - \mathbf{u}_1)(\mathbf{k} \cdot \mathbf{u}_{21})\mathbf{k}$$
$$\times \left[1 - \frac{\sigma_{HS}}{2}\mathbf{k} \cdot \nabla + \cdots + \frac{1}{s!}(-\sigma_{HS}\mathbf{k} \cdot \nabla)^{s-1} + \cdots\right]$$
$$\times W_2(\mathbf{r}, \mathbf{u}_1, \mathbf{r} + \sigma_{HS}\mathbf{k}, \mathbf{u}_2)d\mathbf{k}\, d\mathbf{u}_2\, d\mathbf{u}_1. \qquad (D8)$$

Dropping the subscript for the position, i.e., $\mathbf{r}_1 = \mathbf{r}$, and identifying the mass density as $\rho = mn$, (D6) reduces to the continuum equation for the momentum, namely,

$$\frac{\partial}{\partial t}\langle \rho\mathbf{u}_1\rangle + \nabla_{\mathbf{r}} \cdot \langle \rho\mathbf{u}_1 \otimes \mathbf{u}_1\rangle - \frac{\mathbf{F}}{m} \cdot \langle \rho\rangle = -\nabla_{\mathbf{r}} \cdot \theta(m\mathbf{u}_1). \qquad (D9)$$

It is then possible to identify the kinetic and potential stress tensor as

$$\sigma^k = -\langle \rho(\mathbf{u}_1 - \mathbf{u}) \otimes (\mathbf{u}_1 - \mathbf{u})\rangle,$$
$$\sigma^v = -\theta(m\mathbf{u}_1). \qquad (D10)$$

Finally, using Newton's relation for the viscosity and after some manipulation, one obtains an expression for the viscosity coefficient. The kinetic component of the viscosity is then written as

$$\eta_{HS}^k(y) = \frac{16}{5}\eta^0\rho(y)b^*(y), \qquad (D11)$$

where $\eta^0 = 5(k_B Tm/\pi)^{1/2}/(16\sigma_{HS}^2)$ is the zero-density viscosity.

The potential contribution to the viscosity for a hard sphere fluid is

$$\eta_{HS}^v(y) = \frac{8\pi}{5}\eta^0 \int_{-\sigma_{HS}}^{\sigma_{HS}} y'\sin^3(\arccos(y'))\, I(y, y')\, dy', \qquad (D12)$$

where $I(y, y')$ is given by the infinite series

$$I(y, y') = y'\sum_1^\infty \frac{(-y'^{s-1})}{s!}\frac{\partial^{s-1}}{\partial^{s-1}y}$$
$$\times \left\{g(y, y + y')\rho(y)\rho(y + y')\left[2 + b^*(y + y') + b^*(y)\right]\right\}. \qquad (D13)$$

REFERENCES

[1] Z. Gou and W. Liu, Plant Sci. **172**, 1103 (2007).

[2] J. Bush and D. Hu, Annu. Rev. Fluid Mech. **38**, 339 (2006).

[3] M. H. Nasr, C. E. Green, P. A. Kottke, X. Zhang, T. E. Sarvey, Y. K. Joshi, M. S. Bakir, and A. G. Fedorov, J. Electron. Packag. **139**, 011006 (2017).

[4] R. Peng and D. Li, Microfluid. Nanofluid. **21**, 12 (2017).

[5] B. A. Malouin, N. A. Koratkar, A. H. Hirsa, and Z. Wang, Appl. Phys. Lett. **96**, 234103 (2010).

[6] T. M. Schutzius, G. Graeber, M. Elsharkawy, J. Oreluk, and C. M. Megaridis, Sci. Rep. **4**, 7029 (2014).

[7] T. P. Koukoravas, A. Ghosh, P. S. Mahapatra, R. Ganguly, and C. M. Megaridis, Int. J. Heat Mass Transfer **95**, 142 (2016).

[8] J. E. Sprittles and Y. D. Shikhmurzaev, Phys. Fluids **24**, 082001 (2012).

[9] P. Malgaretti, M. N. Popescu, and S. Dietrich, Soft Matter **12**, 4007 (2016).

[10] C. L. Filomeno, M. Kouyaté, V. Peyre, G. Demouchy, A. F. C. Campos, R. Perzynski, F. A. Tourinho, and E. Dubois, J. Phys. Chem. C **121**, 5539 (2017).

[11] C. Westerhausen, L. G. Schnitzler, D. Wendel, R. Krzysztoń, U. Lächelt, E. Wagner, J. O. Rädler, and A. Wixforth, Micromachines **7**, 150 (2016).

[12] D. Huh, H. J. Kim, J. P. Fraser, D. E. Shea, M. Khan, A. Bahinski, G. A. Hamilton, and D. E. Ingber, Nat. Protoc. **8**, 2135–2157 (2013).

[13] C. Wang, S.-W. Nam, J. M. Cotte, C. V. Jahnes, E. G. Colgan, R. L. Bruce, M. Brink, M. F. Lofaro, J. V. Patel, L. M. Gignac, E. A. Joseph, S. P. Rao, G. Stolovitzky, S. Polonsky, and Q. Lin, Nat. Commun. **8**, 14243 (2017).

[14] R. Sivakumarasamy, R. Hartkamp, B. Siboulet, J.-F. Dufrêche, K. Nishiguchi, A. Fujiwara, and N. Clément, Nat. Mater. **17**, 464 (2018).

[15] H. Craighead, Nature **442**, 387 (2006).

[16] A. Calvo, B. Yameen, F. Williams, G. J. A. A. Soler-Illia, and O. Azzaroni, J. Am. Chem. Soc. **131**, 10866 (2009).

[17] D. M. Heyes, Phys. Rev. B **37**, 5677 (1988).

[18] X.-D. Din and E. E. Michaelides, Phys. Fluids **9**, 3915 (1997).

[19] S. Kjelstrup and D. Bedeaux, *Non-Equilibrium Thermodynamics of Heterogeneous Systems* (World Scientific, 2008).

[20] R. Hartkamp, A. Ghosh, T. Weinhart, and S. Luding, J. Chem. Phys. **137**, 044711 (2012).

[21] H. Hoang and G. Galliero, Phys. Rev. E **86**, 021202 (2012).

[22] B. D. Goddard, A. Nold, N. Savva, G. A. Pavliotis, and S. Kalliadasis, Phys. Rev. Lett. **109**, 120603 (2012).

[23] B. D. Goddard, A. Nold, N. Savva, P. Yatsyshin, and S. Kalliadasis, J. Phys.: Condens. Matter **25**, 035101 (2013).

[24] B. D. Goddard, A. Nold, and S. Kalliadasis, J. Chem. Phys. **145**, 214106 (2016).

[25] J. C. Maxwell, Philos. Mag. **19**, 19 (1860).

[26] R. Liboff, *Kinetic Theory: Classical, Quantum, and Relativistic Descriptions* (Springer, New York, 2003).

[27] S. Chapman, Proc. R. Soc. A **93**, 1 (1916).

[28] D. Enskog, "Kinetische theorie der vorgänge in mässig verdünnten gasen," Ph.D. thesis, Uppsala Universitet, 1917.

[29] D. Enskog, *Kinetische Theorie der Wärmeleitung: Reibung und Selbst-Diffusion in Gewissen Verdichteten Gasen und Flüssigkeiten* (Almqvist & Wiksells boktryckeri-a.-b., 1922).

[30] J. Zhang, B. D. Todd, and K. P. Travis, J. Chem. Phys. **121**, 10778 (2004).

[31] F. Sofos, T. Karakasidis, and A. Liakopoulos, Int. J. Heat Mass Transfer **52**, 735 (2009).

[32] A. Giannakopoulos, F. Sofos, T. Karakasidis, and A. Liakopoulos, Int. J. Heat Mass Transfer **55**, 5087 (2012).

[33] A. E. Giannakopoulos, F. Sofos, T. E. Karakasidis, and A. Liakopoulos, Microfluid. Nanofluid. **17**, 1011 (2014).

[34] H. Hoang and G. Galliero, J. Chem. Phys. **136**, 124902 (2012).

[35] H. Hoang and G. Galliero, J. Phys.: Condens. Matter **25**, 485001 (2013).

[36] M. Morciano, M. Fasano, A. Nold, C. Braga, P. Yatsyshin, B. D. Goddard, E. Chiavazzo, P. Asinari, and S. Kalliadasis, J. Chem. Phys. **146**, 244507 (2017).

[37] P. A. Thompson and M. O. Robbins, Phys. Rev. A **41**, 6830 (1990).

[38] R. Hartkamp, B. D. Todd, and S. Luding, J. Chem. Phys. **138**, 244508 (2013).

[39] R. Kamali and A. Kharazmi, Int. J. Therm. Sci. **50**, 226 (2011).

[40] B. D. Todd and D. J. Evans, Phys. Rev. E **55**, 2800 (1997).

[41] A. G. Goicochea, E. Mayoral, J. Klapp, and C. Pastorino, Soft Matter **10**, 166 (2014).

[42] K. Travis, B. Todd, and D. Evans, Phys. Rev. E **55**, 4288 (1997).

[43] C. Soong, T. Yen, and P. Tzeng, Phys. Rev. E **76**, 036303 (2007).

[44] Q. Li and C. Liu, Int. J. Heat Mass Transfer **55**, 8088 (2012).

[45] X. Yong and L. T. Zhang, J. Chem. Phys. **138**, 084503 (2013).

[46] S. Nosé, J. Chem. Phys. **81**, 511 (1984).

[47] S. Nosé, Mol. Phys. **52**, 255 (1984).

[48] W. G. Hoover, Phys. Rev. A **31**, 1695 (1985).

[49] S. Li and N. Sheng, Int. J. Numer. Methods Eng. **83**, 998 (2010).

[50] S. Plimpton, J. Comput. Phys. **117**, 1 (1995).

[51] L. Verlet, Phys. Rev. **159**, 98 (1967).

[52] P. A. Thompson and S. M. Troian, Nature **389**, 360 (1997).

[53] L. B. Lucy, Astron. J. **82**, 1013 (1977).

[54] J. M. Vanegas, A. Torres-Sánchez, and M. Arroyo, J. Chem. Theory Comput. **10**, 691 (2014).

[55] J. A. Zimmerman, E. B. Webb III, J. J. Hoyt, R. E. Jones, P. A. Klein, and D. J. Bammann, Modell. Simul. Mater. Sci. Eng. **12**, S319 (2004).

[56] T. Belytschko, Y. Krongauz, D. Organ, M. Fleming, and P. Krysl, Comput. Methods Appl. Mech. Eng. **139**, 3 (1996).

[57] T. Weinhart, R. Hartkamp, A. R. Thornton, and S. Luding, Phys. Fluids **25**, 070605 (2013).

[58] I. Goldhirsch, Granular Matter **12**, 239 (2010).

[59] W. G. Hoover, C. G. Hoover, and J. F. Lutsko, Phys. Rev. E **79**, 036709 (2009).

[60] S. N. Atluri and S. Shen, Adv. Comput. Math. **23**, 73 (2005).

[61] G. J. Wang and N. G. Hadjiconstantinou, Phys. Rev. Fluids **2**, 094201 (2017).

[62] W. Noll, J. Ration. Mech. Anal. **4**, 627 (1955).

[63] P. Schofield and J. R. Henderson, Proc. R. Soc. A **379**, 231 (1982).

[64] N. C. Admal and E. B. Tadmor, J. Elasticity **100**, 63 (2010).

[65] R. Hartkamp and S. Luding, in *7th International Conference on Multiphase Flow*, edited by Nuernberg MesseGmbH (Nuernberg Messe GmbH, 2010), pp. 1–7.

[66] E. Chiavazzo, M. Fasano, P. Asinari, and P. Decuzzi, Nat. Commun. **5**, 3565 (2014).

[67] L. Joly, C. Ybert, E. Trizac, and L. Bocquet, Phys. Rev. Lett. **93**, 257805 (2004).

[68] P.-A. Cazade, R. Hartkamp, and B. Coasne, J. Phys. Chem. C **118**, 5061 (2014).

[69] A. Sam, R. Hartkamp, S. K. Kannam, and S. P. Sathian, Nanotechnology **29**, 485404 (2018).

[70] J. Fischer and M. Methfessel, Phys. Rev. A **22**, 2836 (1980).

[71] N. F. Carnahan and K. E. Starling, J. Chem. Phys. **51**, 635 (1969).

[72] S. Morioka, J. Non-Cryst. Solids **341**, 46 (2004).

[73] J. O. Hirschfelder, C. F. Curtiss, and R. B. Bird, *Molecular Theory of Gases and Liquids* (Wiley, New York, 1954).

[74] P. D. Neufeld, A. R. Janzen, and R. A. Aziz, J. Chem. Phys. **57**, 1100 (1972).

[75] I. Bitsanis, J. J. Magda, M. Tirrell, and H. T. Davis, J. Chem. Phys. **87**, 1733 (1987).

[76] G. Galliéro, C. Boned, and A. Baylaucq, Ind. Eng. Chem. Res. **44**, 6963 (2005).

[77] A. Liakopoulos, F. Sofos, and T. E. Karakasidis, Phys. Fluids **29**, 052003 (2017).

[78] S. K. P. Sanjeevi, A. Zarghami, and J. T. Padding, Phys. Rev. E **97**, 043305 (2018).

[79] C. Braga, E. R. Smith, A. Nold, D. N. Sibley, and S. Kalliadasis, J. Chem. Phys. **149**, 044705 (2018).

[80] T. Schneider and E. Stoll, Phys. Rev. B **17**, 1302 (1978).

[81] T. Soddemann, B. Dünweg, and K. Kremer, Phys. Rev. E **68**, 046702 (2003).

[82] B. L. Holian, A. F. Voter, and R. Ravelo, Phys. Rev. E **52**, 2338 (1995).

[83] S. Hess, Int. J. Thermophys. **23**, 905 (2002).

[84] H. V. Beijeren and M. Ernst, Physica **68**, 437 (1973).